JOURNAL OF GEOPHYSICAL RESEARCH, VOL. 96, NO. C8, PAGES 14,959–14,977, AUGUST 15, 1991

Dynamics of the Coastal Transition Zone Through Data Assimilation Studies

LEONARD J. WALSTAD, J. S. ALLEN, P. MICHAEL KOSRO, AND ADRIANA HUYER

College of Oceangraphy, Oregon State University, Corvallis

The dynamics of the coastal transition zone off Northern California during late May and early June 1987 are examined through assimilation modeling studies. A regional baroclinic quasi-geostrophic model is driven by the data through initial and boundary conditions. These initial and boundary conditions are specified by objective analysis of hydrographic and acoustic Doppler current profiler data. The data assimilation is accomplished by varying the objective analysis parameters, numerical parameters, and subgrid-scale parameters until the final solution of the model is in best agreement with the analysis of the data. The solution which best agrees with the data is regarded as a four dimensional field estimate of the coastal transition zone flow. An aspect of this study that is new to data assimilation modeling of mesoscale eddy fields is the use of acoustic Doppler current profiler data. These data prove to be very important to accurate description of the oceanic flow field as indicated by comparison with float trajectories. The complete data set provides an opportunity to study the ability of dynamical constraints to improve field estimates when acting upon a subset of the data (hydrography). Data assimilation modeling generates field estimates that are substantially better than those based upon the hydrographic data alone as indicated by comparison with the acoustic Doppler current profiler based analyses. The kinematics and energetics of this constrained (quasi-geostrophic) field estimate are examined. Despite the relatively small region (108 by 324 km) and short period of the field estimate (21 days), interesting processes are identified. A meandering barotropically unstable part of the jet is identified using the results of related idealized numerical studies and stability analyses. Similarly, this jet may be undergoing a simultaneous larger scale mixed instability. Another part of the jet interacts with an eddy and meanders in a much different manner. Characteristics of the energy balances are identified and compared with the results of linear analysis and of nonlinear studies utilizing idealized models of the observed jet as described in this issue by Pierce et al. and Allen et al. respectively.

1. INTRODUCTION

The presence of energetic mesoscale jets and eddies has been identified as a persistent feature of the California Current system during late spring and summer [*Strub et al.*, this issue; *Mooers and Robinson*, 1984]. The Coastal Transition Zone (CTZ) experiment focused observational resources on the inshore edge of this system in 1987 and 1988 [*Kosro et al.*, this issue; *Huyer et al.*, this issue]. The shelf is 50 to 100 km wide (Figure 1) and inshore surface temperatures are generally cold as a result of upwelling [*Huyer*, 1984; *Flament et al.*, 1985]. An understanding of the structure of the CTZ currents has emerged from the CTZ program: a strongly baroclinic jet meanders along the coast, carrying both fresh water from north of the region and cold salty upwelled water from inshore [*Strub et al.*, this issue], and interacts with an eddy field in ways not understood. An understanding of the source of energy for the jet meanders and the interaction of the jet with the eddy fields is needed. Direct dynamical analysis of the survey data is not possible, largely because of the lack of synopticity during surveys and the time elapsed between surveys. CTZ features evolve with time scales of several weeks; thus field estimates based upon week-long shipboard surveys are moderately affected. Substantial changes can occur between surveys. The dynamics of intense jets and eddies are significantly nonlinear such that an analysis of the dynamics must be carried out on fields which fully resolve the evolving flow.

Assimilation modeling has been used successfully to provide the needed interpolation between successive surveys in the California Current [*Rienecker et al.*, 1987] and elsewhere [*Walstad and Robinson*, 1990; *Robinson et al.*, 1988; *Carton*, 1987]. The assimilation modeling procedure uses data-based initial and boundary conditions in a dynamical model. The inshore edge of our study domain is approximately located along the outer edge of the continental slope (Figure 1). While measurements were also taken farther to the north (Figure 2), the northern portion of the cruise track varied between the two surveys. The chosen domain represents the largest rectangular area with data from both cruises. Data are objectively analyzed to provide the initial and boundary conditions and the fields with which the model solutions are compared. In the case of two surveys, objective analysis of the data from the first provides the initial conditions. Comparison of the model solution for the time of the second survey with the analysis of the second survey data indicates how well the model fields are representing the ocean. A new aspect of these studies is the use of acoustic Doppler current profiler (ADCP) measurements [*Kosro et al.*, this issue] to provide the absolute velocity data need for initial, boundary, and comparison fields.

The parameters which control the interpolation of the data, the subgrid-scale dissipation of the numerical model, and the resolution used to numerically solve the model equations are varied to explore the dependence of the model solutions upon parameter space and to approach the best possible agreement between model and data. This procedure is data assimilation in that measurements are used to constrain the solution and that the initial and boundary conditions are varied to obtain improved agreement between model and data analyses. The resulting solution, consisting typically of hourly fields, provides a constrained interpolation of the data, and the final solution may be a better field estimate than a simple objective analysis of the survey data. This capability for improving field estimates is addressed by comparing the field estimates produced by assimilation modeling with only hydrographic data to the field estimates made by an analysis of the full hydrographic and ADCP data set.

Pinardi and Robinson [1986] developed a method for analyzing the energy and vorticity dynamics of quasi-geostrophic flows in limited regions. This method provides maps of the terms in the energy and vorticity equations and also relates QG energy

Copyright 1991 by the American Geophysical Union.

Paper number 91JC01022.
0148–0227/91/91JC-01022$05.00

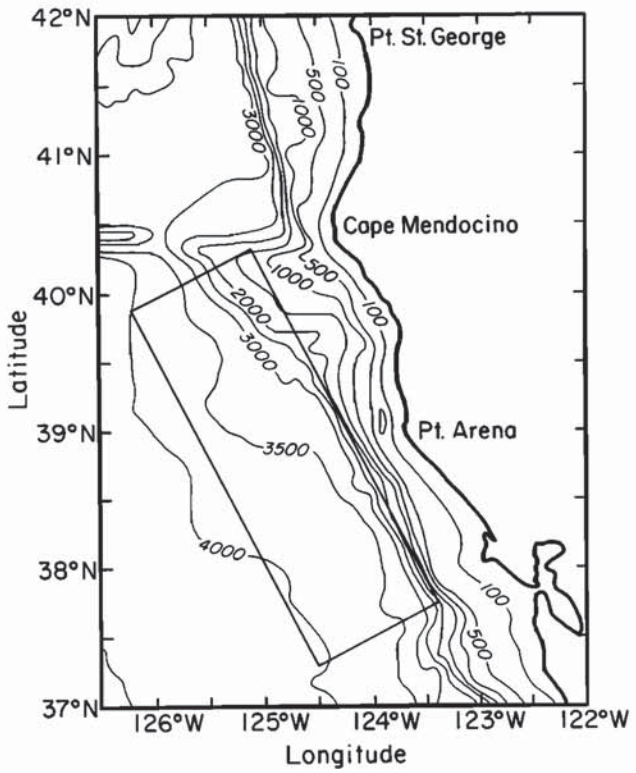

Fig. 1. Bottom topography of the Coastal Transition Zone experiment region with the model domain indicated.

terms to their primitive equation counterparts which aids in the interpretation of flow dynamics. This method was applied to the best model solution and used in conjunction with linear stability analysis and idealized numerical studies of the CTZ jet [*Pierce et al.*, this issue; *Allen et al.*, this issue] to determine the dynamics in the CTZ during the late spring of 1987.

The objective of this study is to describe the CTZ flow during late spring of 1987 using data assimilation modeling. Energetics of the jet and eddy system are used to identify fundamental processes and relate this complex flow to idealized flow studies. We begin with a description of the data assimilation method and the data in section 2. Then we consider the assimilation experiments and the dependence of the model solution on parameters of the analysis and numerics in section 3. Section 4 presents an analysis of the model solution which best agrees with the survey data. Kinematic and dynamic analysis of the model solution indicates the processes which control evolution of the fields. A discussion of the applicability of these findings to the coastal transition zone concludes the paper.

2. Physical Model, Data, and Analysis

Physical Model

The physical model used in this study is a regional quasi-geostrophic, open-ocean model of which the computational characteristics have been well documented [*Haidvogel et al.*, 1980; *Miller et al.*, 1981; *Robinson and Walstad*, 1987]. The dimensionless quasi-geostrophic (QG) equations are

$$\frac{D}{Dt}Q + \beta\psi_x = F_{pqr}Q, \tag{1a}$$

$$Q = \zeta + \Gamma^2(\sigma\psi_z)_z, \qquad \zeta = \nabla^2\psi, \tag{1b}$$

$$\frac{D}{Dt}\psi_z = F_{pqr}\psi_z - \frac{D\hat{k}\cdot\nabla\times(\vec{\tau}/f)}{\epsilon V_0 H\Gamma^2\sigma} \quad \text{at } z=0, \tag{1c}$$

$$\frac{D}{Dt}\psi_z = F_{pqr}\psi_z + \frac{J(\psi, z_b)}{\epsilon H\Gamma^2\sigma} \quad \text{at } z=-H, \tag{1d}$$

where ψ is the QG stream function, $u=-\psi_y$ and $v=\psi_x$ are the geostrophic velocity components, Q is the quasi-geostrophic potential vorticity, and $\frac{D}{Dt}=\frac{\partial\cdot}{\partial t}+\alpha J(\psi,\cdot)$. The parameters are $\alpha = V_0 t_0 D^{-1}$, $\beta = \beta^* t_0 D$, $\Gamma^2 = f_0^2 D^2/N_0^2 H^2$, and $\sigma = N_0^2/\overline{N^2}(z)$, which are determined by the regional mean Coriolis parameter, $f_0 = 2\Omega\sin\Theta_0$; the regional mean gradient of the Coriolis parameter, $\beta^* = R^{-1}2\Omega\cos\Theta_0$, and the regional mean Brunt-Väisälä frequency-squared profile, $\overline{N^2}(z)$; and the scales used to nondimensionalize the equations and solution: horizontal velocity, V_0; horizontal length scale, D; vertical length scale, H; typical Brunt-Väisälä frequency, N_0; and time scale, t_0. The wind stress is $\vec{\tau}$, and the bottom height is z_b. Additionally, R is the radius of the Earth, Ω is the rotation rate of the Earth, and Θ_0 is the latitude of the center of the region. Subgrid-scale dissipation is parameterized by a Shapiro filter, F_{pqr}, of order p, applied q times every r time steps [*Shapiro*, 1970]. This is a low-pass filter intended to remove wavelengths of twice the grid spacing; higher-order Shapiro filters remove less of the longer wavelengths.

The regional mean profiles of temperature, salinity, dynamic height, and Brunt-Väisälä frequency squared $\left(\overline{T}(z),\ \overline{S}(z),\ \overline{\Delta D}(z),\ \text{and}\ \overline{N^2}(z)\right)$ were obtained by calculating temporal and horizontal averages based upon the May–June 1987 CTZ data set within 50 km of the model domain, except below 500 m where there were no measurements. Conductivity-temperature-depth (CTD) measurements made to within 10 m of the bottom during July 1985 at mooring locations southwest of Point Arena between 3500 and 4000 m depth [*Smith et al.*, 1986] were used to derive the deep mean profiles. While deep data from the time of the CTZ surveys would be preferred, the variability in the deep ocean is weak and we observed that the deep and upper ocean mean profiles met smoothly at 500 m depth. The Rossby radius of the first baroclinic mode calculated from the $\overline{N^2}$ profile is 24.6 km, less than one quarter of the narrowest dimension of the model domain (108 by 324 km).

The numerics of the model are finite element for solution of the prognostic pseudo-potential vorticity equation, surface and bottom buoyancy equations (eqns. (1a), (1c), and (1d)) and finite difference for solution of the elliptic boundary value problem (eqn. (1b)) [*Robinson and Walstad*, 1987]. The horizontal model grid spacing is uniform in the x and y directions; vertical grid spacing is arbitrary. The standard model resolution will be 9 km in the horizontal and six levels in the vertical, with four levels concentrated in the upper 500 m. These finite element solutions with 9-km resolution are comparable to second-order finite difference solutions with 4.5-km resolution as indicated by the model intercomparisons of *Haidvogel et al.* [1980].

Quasi-geostrophy is an approximation to the generally accepted primitive equations when the Rossby number ϵ is small and the scaled solution remains $O(1)$. Small is a relative term and best defined by considering the neglected terms. A perturbation expansion in Rossby number may be used to derive the quasi-geostrophic equations; geostrophy is the lowest-order balance, quasi-geostrophy enters as a vorticity balance in the first-order equations. Terms which are $O(\epsilon^2)$ are neglected in the vorticity balance; however, the terms retained in the vorticity balance are $O(\epsilon)$. The importance of maintaining a solution which is $O(1)$ is that this indicates that the chosen scaling is correct throughout

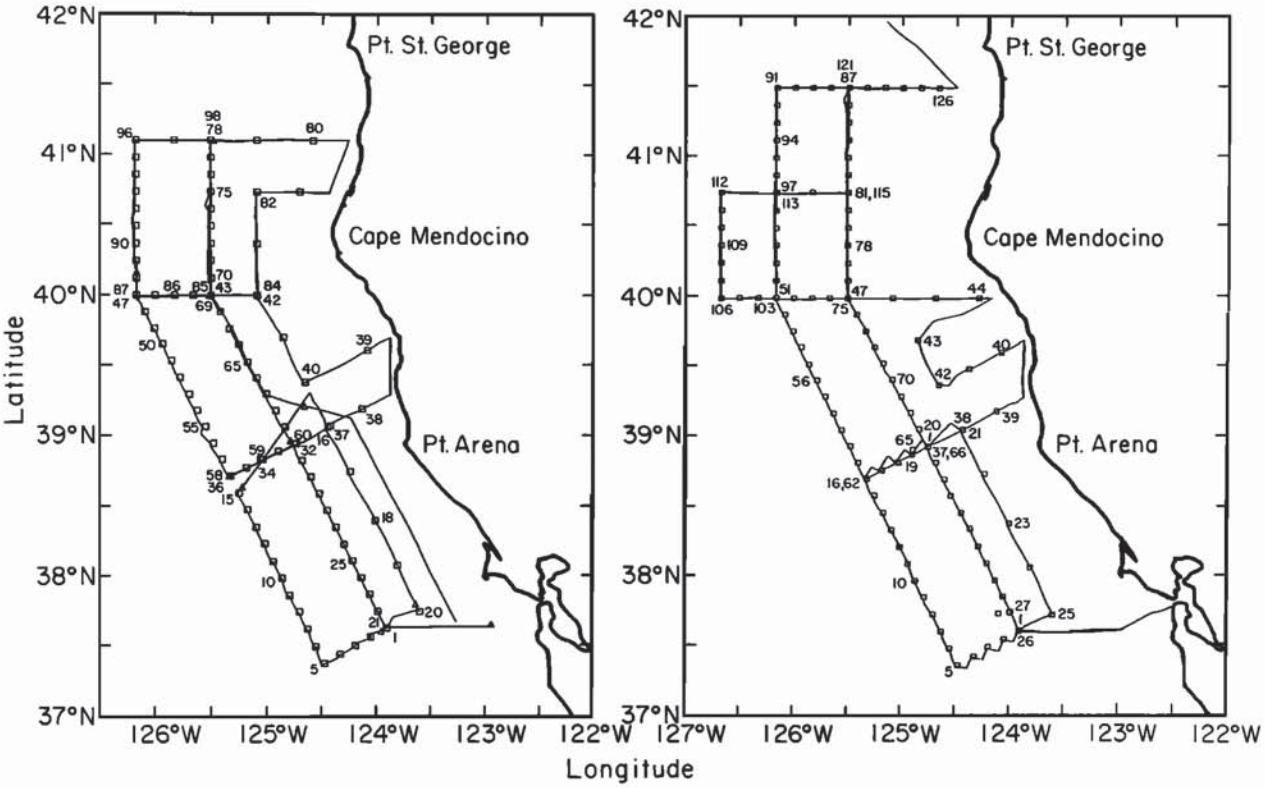

Fig. 2. Track of the May 18–27 and June 9–18, 1987 cruises [*Kosro et al.*, this issue]. Boxes indicate hydrographic stations; station numbers are indicated for every fifth station and where needed for clarity.

the solution. Topographic forcing is one mechanism which may force the solution to be other than $O(1)$. A simple means for insuring that topography does not directly force the solution to violate the scaling is to insure that the topographic slopes are $O(\epsilon H D^{-1})$; then the vertical velocity at the bottom, which forces equation (1c), will be $O(\epsilon)$. However, this is a very strong restriction. The fundamental limitation is that the vertical velocity be of order the Rossby number; $w \leq O(\epsilon)$. The local Rossby number indicates the amplitude of neglected terms in the vorticity balance. A good measure of the local Rossby number is ζ^*/f_0, where the asterisk superscript indicates a dimensional variable. No limit to the amplitude of the Rossby number is known and the applicability of quasi-geostrophy to flows with large Rossby numbers is an open question.

The Data Set

The data set used in these studies consists of CTD stations to at least 495 m and ADCP data at 97, 121, and 146 m depth. The first cruise from which data were used in this study, May 18–27, 1987, provided 76 hydrographic stations and approximately 140 ADCP velocity measurements at each of the three depths after processing [*Kosro et al.*, this issue]. The second cruise, June 9–18, 1987, also provided 76 hydrographic stations and approximately 160 ADCP velocity measurements at each of these depths. The hydrographic data is a subset of the collected data; profiles to less than 495 m were neglected. The locations of the hydrographic stations are shown in Figure 2. Velocity measurements and their locations are shown in Figure 3. Results from these cruises are described by *Kosro et al.* [this issue].

When combined, the hydrographic and ADCP measurements determine the flow field in the upper 500 m. Dynamic height is approximately the quasi-geostrophic stream function at the surface relative to depth z after removal of the mean and the appropriate change of units:

$$\psi^*(x,y,z,t) - \psi^*(x,y,0,t) \approx \frac{-g}{f_0}\left(\Delta D(x,y,z,t) - \overline{\Delta D}(z)\right) = \frac{-g}{f_0}\Delta \dot{D}(x,y,z,t), \quad (2)$$

where ψ^* is the dimensional quasi-geostrophic stream function and ΔD is surface dynamic height relative to depth z [*Robinson and Walstad*, 1987]. The approximation arises because of slight differences between pressure on level surfaces and geopotential height on constant pressure surfaces and is consistent with the quasi-geostrophic approximation. The relationship between QG stream function and ADCP velocities is less direct. While any field of dynamic height may be scaled to provide a QG relative stream function field, the geostrophic velocity must be nondivergent, since it is described by a stream function. In general, if u_s and v_s are the ADCP-sampled velocities, then $\psi^*_x \neq v_s$ and $\psi^*_y \neq -u_s$. The divergence in the data set must be removed. This may be accomplished either by applying a gridding algorithm which enforces nondivergence [*Bretherton et al.*, 1976] or through removal of the divergent component of the velocity field after gridding [*Carter and Robinson*, 1987]. We utilize the former procedure here.

Analysis of Dynamic Height Data

The numerical model requires gridded values of stream function and vorticity for initial and boundary conditions. Relative stream function was estimated on a rectangular Cartesian coordinate

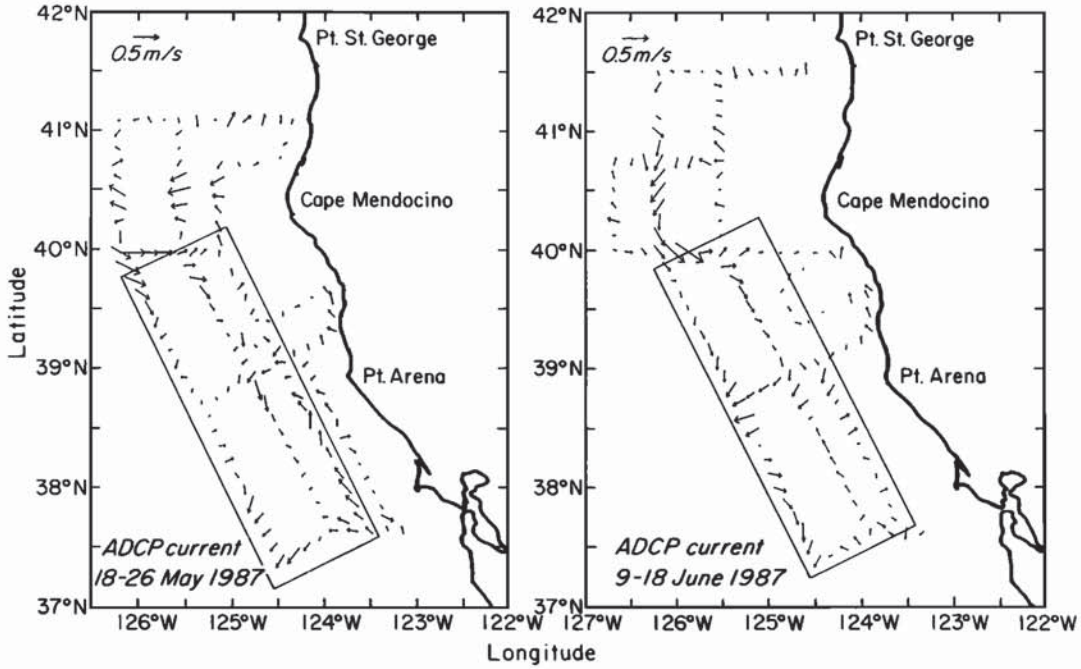

Fig. 3. Current at 97 m as measured by the shipboard acoustic Doppler current profiler on May 18–26 and June 9–18, 1987 [*Kosro et al.*, this issue]. The model domain is indicated by the rectangle.

$(x-y)$ grid that is one grid point larger on each side than the grid used by the numerical model. This allows calculation of relative vorticity with a centered difference operator at all model grid points. Experience has shown this approach to be preferable to using a one-sided difference operator at the boundary [*Walstad and Robinson*, 1990]. The grid is centered at 38.8°N, 124.8°W, has the y axis rotated 27° counterclockwise from north, is 108 km in the x direction and 324 km in the y direction, and is shown in Figure 1. The number of levels and the horizontal resolution are varied to study the effects of the numerical parameters. Table 1 indicates the resolutions that were used. As was noted above, most of the analyses are performed using parameters from grid i with $\Delta x = 9$ km and from level i with six levels.

Field estimates of dynamic height at the surface relative to all model levels above 495 m and at the surface relative to 495 m (i.e., 50, 150, 250, and 495 m for the level i model) are calculated for each cruise. Pairs of nonindependent data are first removed from the data set by averaging their positions, times, and values. A pair of data is independent if their correlation (see below) is less than 0.98. The linear (least squares) trend at each vertical level is then removed from this reduced data set. Standard objective analysis as described by *Bretherton et al.* [1976] is applied to the detrended data at each level. The objectively analyzed detrended estimate for each grid point is then summed with the value of the linear trend at that grid point to produce the dynamic height estimate.

Objective analysis requires specification of the normalized uncorrelated error variance, ϵ^2, and of the correlation, defined for variables ω and π as

$$C_{\omega\pi}(\Delta x, \Delta y) = \frac{\int_A (\omega(x+\Delta x, y+\Delta y) - \bar{\omega})(\pi(x,y) - \bar{\pi})\, dA}{\left(\int_A (\omega - \bar{\omega})^2\, dA \int_A (\pi - \bar{\pi})^2\, dA\right)^{1/2}}, \quad (3)$$

here assumed to be homogeneous. The relatively small data set precluded directly calculating an accurate correlation function. A two parameter isotropic functional form,

$$C_{\Delta D\,\Delta D}(r^2 = \Delta x^2 + \Delta y^2) = \left(1 - \frac{r^2}{b^2}\right) e^{-(r/a)^2} \quad (4)$$

was assumed for the dynamic height (and stream function) and

TABLE 1. The Varied Numerical Parameters and Parameter Set Identifiers

Parameter Set Identifier	Δt, days	α	β
I	0.05	1.00	0.111749
II	0.025		
III	0.0125		
IV	0.025	0.00	
V	0.025	1.00	0.00
VI	0.025	0.00	

Level Set Identifier	l	Level Depths, m
i	6	50, 150, 250, 500, 1100, 2336
ii	12	24, 79, 150, 243, 363, 520, 724, 988, 1332, 1780, 2318, 2887

Grid Identifier	m	n	Resolution, km
i	13	37	9
ii	19	55	6

TABLE 2. Objective Analysis Correlation Function Parameter Sets

Objective Analysis Parameter Set Identifier	a, km	b, km
A	50	60
B	50	75
C	50	90
D	40	60
E	60	75
F	70	75

numerical experiments were performed to determine the most appropriate value for the decay scale a, and the zero crossing b. These parameters are subject to the restriction that the zero crossing must be larger than the decay scale ($a < b$) [*Denman and Freeland*, 1985]. Table 2 lists the parameter combinations which were used in this study. The uncorrelated error has been assumed to be 10% of the variance in the dynamic height at each level. For the data from each cruise, the correlation function is assumed independent of time and the field estimate is produced for the midpoint of the cruise; May 22, and June 12. An example of the objectively analyzed dynamic height fields may be seen in Figure 4.

As field estimates are needed throughout the water column, the dynamic height must be extrapolated to model levels below 495 m (i.e., 500, 1100, and 2336 m of the level i model). In some regions of the ocean, like the MODE region of the northwest Atlantic [*Richman et al.*, 1977] and the OPTOMA region off northern California [*Smith et al.*, 1985], ocean variability exhibits strong vertical coherence. This property is assumed here and is exploited by fitting and extrapolating the dominant vertical function. Since the CTZ program included no deep measurements, we used the first baroclinic mode for fitting and extrapolating. The first-baroclinic-mode structure was calculated from the regional mean density profile by a shooting method on a 20-m grid; centered differences of this mode provided vertical shear values at 20-m intervals. First-baroclinic-mode amplitudes for each CTZ hydrographic profile were determined by interpolating the dynamic height data to the same depths as the regional baroclinic mode profile, removing the horizontal-temporal mean dynamic height at each depth, applying centered differences to obtain the vertical shear, and finally by least squares fitting the profile of first-baroclinic-mode shear to the shear of the demeaned dynamic height. The fitting interval is limited to the the depth range 200–480 m to reduce the errors introduced by structures in the upper ocean such as the surface mixed layer. Experiments with shallower upper limits (to 100 m) showed little sensitivity. The mode amplitudes are then objectively analyzed using the same procedure employed for gridding the dynamic height values (Figure 4).

Analysis of Acoustic Doppler Current Profiler Data

Absolute velocity measurements provided by the acoustic Doppler current profiler are of great benefit here, since knowledge of the absolute geostrophic velocity field eliminates the need to assume a level of no motion when estimating QG stream function, however significant measurement and system (ageostrophic) noise is expected in these velocity estimates, so they must be used with care. ADCP data from the two cruises were processed by *Kosro et al.* [this issue] to produce absolute velocities. The processing involved addition of navigation data to make velocities absolute and time averaging to reduce errors. As the measurements are made continuously along the ship track, short-period motions (i.e., tidal) are not separable from the slowly varying velocity field of interest; the steaming of the ship aliases the tidal and inertial

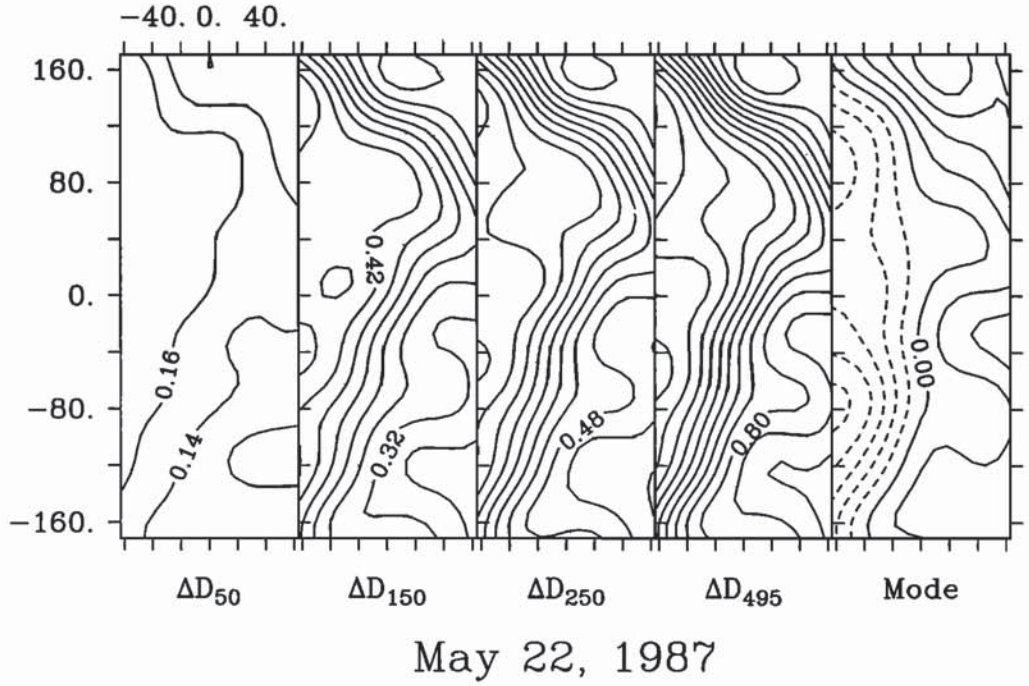

Fig. 4. Objectively analyzed dynamic height and first baroclinic mode amplitude for May 22 (correlation parameter set A; a = 50 km, b = 60 km).

signals into the mesoscale eddy velocity field. However, the smoothing and nondivergence enforced by the objective analysis described below is expected to reduce these errors. The horizontal velocities at 97, 121, and 146 m depth were objectively analyzed to determine absolute stream function at these three depths (Figure 5).

Objective analysis is applied to the velocity data from each cruise with the regional-mean velocity from that cruise removed. Data from each of the three depths are analyzed separately; yielding a field estimate for each depth. This procedure is consistent with geostrophy and with the dynamic height analysis in which the linear trend is removed. Objective analysis of the residual velocities to absolute stream function [*Bretherton et al.*, 1976] requires specification of five correlations which are derived from the dynamic height correlation $C_{\Delta D\,\Delta D}$ (eqn (4)), and the geostrophic relationship:

$$C_{u\,u} = \frac{\Delta x^2}{r^2}\left(R(r) - S(r)\right) + S(r),$$

$$C_{v\,v} = \frac{\Delta y^2}{r^2}\left(R(r) - S(r)\right) + S(r),$$

$$C_{u\,v} = \frac{\Delta x\,\Delta y}{r^2}\left(R(r) - S(r)\right),$$

$$C_{u\,\psi} = \frac{g}{f_0}\Delta y\,R(r),$$

and

$$C_{v\,\psi} = \frac{-g}{f_0}\Delta x\,R(r) \tag{5}$$

with

$$R(r) = \frac{2}{a^2 b^2}\left(a^2 + b^2 - r^2\right)e^{-r^2/a^2},$$

and

$$S(r) = \frac{2}{a^2 b^2}\times \left(a^2 + b^2 - \left(5.0 + \frac{2}{a^2}\left(b^2 - r^2\right)\right)r^2\right)e^{-r^2/a^2}.$$

The residual absolute stream function is estimated at each grid point and combined with the mean absolute stream function to obtain the absolute stream function,

$$\psi^*(x, y, z_{\mathrm{ADCP}}, t) = L[\acute{u}, \acute{v}] + \tilde{v}x - \tilde{u}y, \tag{6}$$

where L represents the linear operator which is objective analysis acting upon the array of velocity residuals, $[\acute{u}, \acute{v}] = [\acute{u}_i, \acute{v}_i]$, defined as

$$\acute{u}_i = u(x_i, y_i, z_{\mathrm{ADCP}}, t_i) - \tilde{u}\left(z_{\mathrm{ADCP}}, \tilde{t}_i\right),$$
$$\acute{v}_i = v(x_i, y_i, z_{\mathrm{ADCP}}, t_i) - \tilde{v}\left(z_{\mathrm{ADCP}}, \tilde{t}_i\right), \tag{7}$$

with the measurements (u_i, v_i) and the horizontal-mean velocities $(\tilde{u}, \tilde{v})$, where $(\tilde{\cdot}) = 1/A\int dA$ indicates the horizontal mean within 50 km of the model domain. When averaging measurements, we consider all data during a single survey to be synoptic; there are separate horizontal-mean velocities for each cruise. The horizontal-mean velocity provides the mean slope in the dynamic topography as represented by the last two terms in equation (6), through application of the geostrophic relationship.

Constructing Stream Function

Once maps of relative stream function have been constructed, there are several methods for generating absolute stream function. The simplest is to use a level-of-no-motion (LNM) assumption to set the flow fields to zero at a particular depth, $\psi^*(x, y, z_{\mathrm{LNM}}, t) = 0$. To obtain the stream function in the full water column, simply remove a barotropic field and rescale:

$$\psi^*(x, y, z, t) = \frac{g}{f_0}\left(\Delta\acute{D}(x, y, z_{\mathrm{LNM}}, t) - \Delta\acute{D}(x, y, z, t)\right) \tag{8}$$

where z_{LNM} is the level-of-no-motion depth. An example of these fields for a 700-m level of no motion may be seen in Figure 6. An alternative approach is to use a depth of no motion (DNM), which is a function of space and time. While not immediately obvious, oceanic flows that reverse direction between the surface and the bottom need not have a DNM. Rather, the flow may rotate with depth. Without additional data, specifying the DNM would simply add additional degrees of freedom to the analysis procedure. In the absence of absolute velocity data, this is a reasonable approach to developing the best possible model fields. Here, our intention is to assess the LNM approach which has been used in past studies.

The LNM assumption is avoided by using the ADCP-specified stream function at the ADCP data depth combined with the dynamic height fields;

$$\psi^*(x, y, z, t) = \psi^*(x, y, z_{\mathrm{ADCP}}, t) + \frac{g}{f_0}\left(\Delta\acute{D}(x, y, z_{\mathrm{ADCP}}, t) - \Delta\acute{D}(x, y, z, t)\right) \tag{9}$$

where z_{ADCP} is the depth of the ADCP data being used. An example of these fields using the 97-m ADCP data may be seen in Figure 7. The following figure, Figure 8, is the relative vorticity, ζ, of the 50-m stream function fields on May 22 and June 12. Note that for a substantial portion of the domain $-0.3f_0 < \zeta < 0.3f_0$.

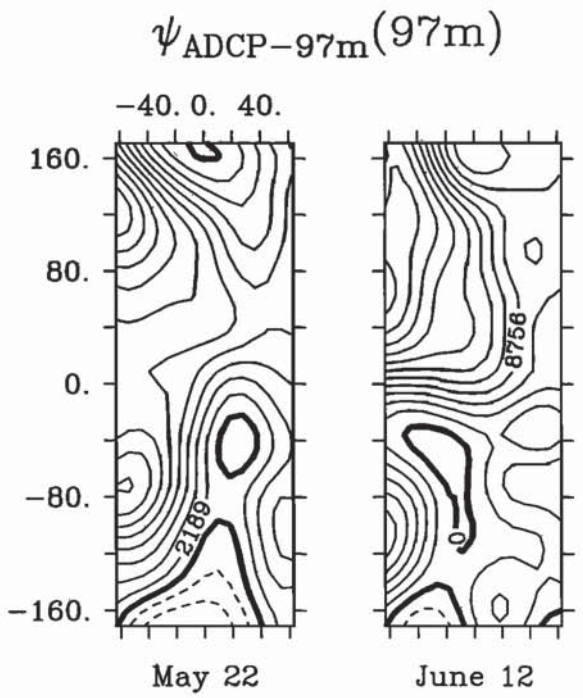

Fig. 5. Stream function at 97 m depth on May 22 and June 12, 1987, as objectively analyzed from the acoustic Doppler current profiler measurements (a = 50 km, b = 60 km). Contour interval is equivalent to 2 dyn. cm. The rectangle is the model domain; tick spacing is 25 km.

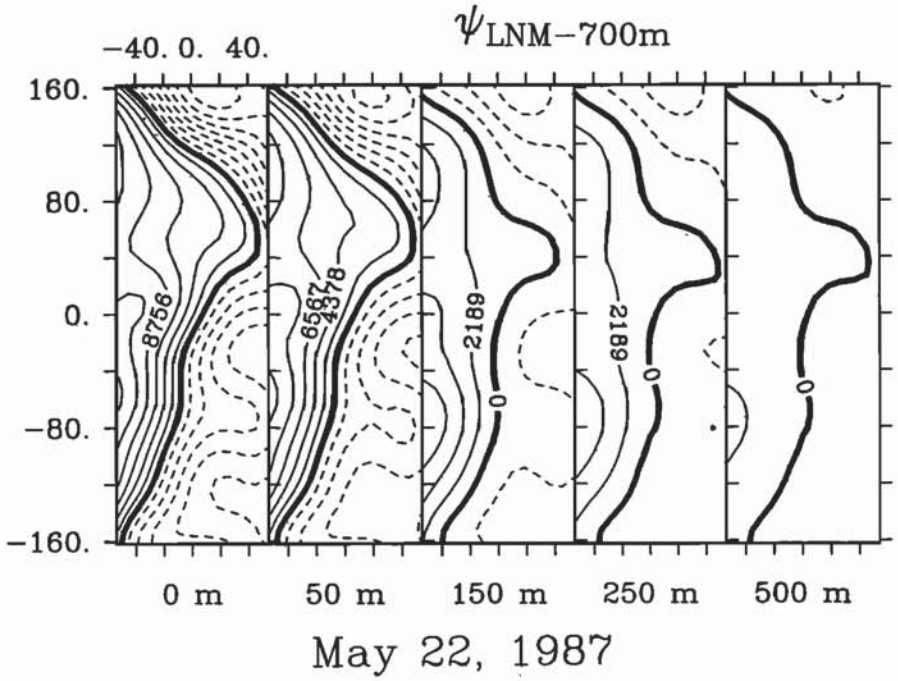

Fig. 6. LNM stream function analysis fields based on a level of no motion at 700 m depth for depths of 0, 50, 150, 250, and 500 m on May 22, 1987. Objective analysis parameters are $a = 50$ km and $b = 60$ km. Contour interval is equivalent to 2 dyn. cm.

Intercomparison of Analyses and Comparison with Independent Data

In this study, absolute stream function is available and may be compared with the LNM analyses to explore the effects of the LNM approximation. There are drifter data from releases made on and about May 19, 1987, which are used to assess the reliability of the absolute stream function relative to the LNM stream function. We focus upon the May 22 analyses, since the drifters were in the region at that time. The stream function for May 22 with a 700-m LNM and that with ADCP data indicate that the differences are significant (Figures 6 and 7). Both stream function analyses indicate a southward flowing jet with flow onshore in the northern third of the domain and offshore in the southern two thirds. Primary differences are seen in the eddies north of the jet and west of the jet and in the region east of the jet. LNM stream function indicates a weak eddy to the north of the jet (2 dyn. cm),

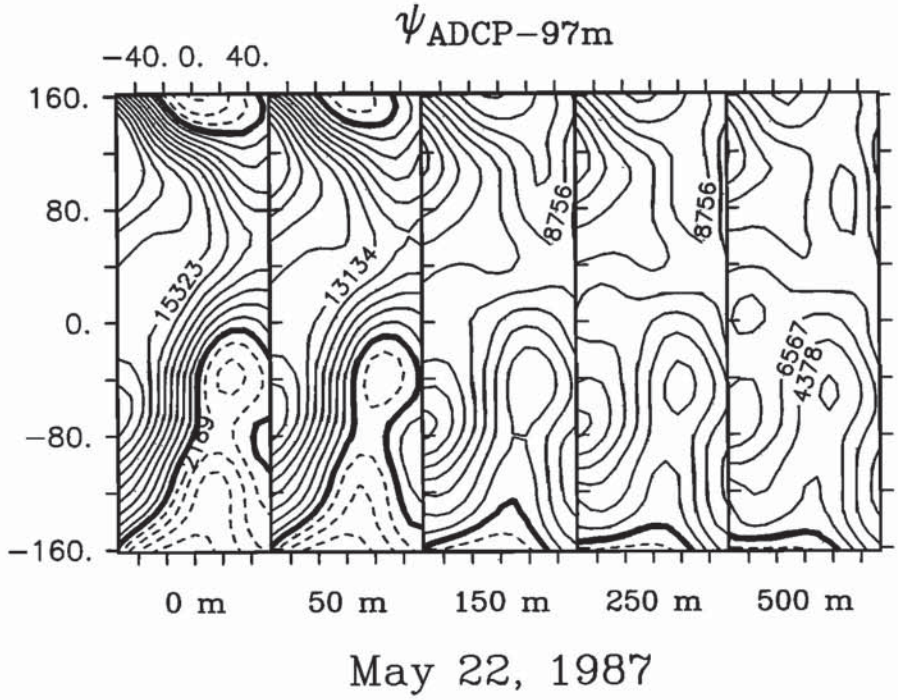

Fig. 7. Absolute stream function analysis fields based on ADCP data at 97 m depth for depths of 0, 50, 150, 250, and 500 m on May 22, 1987. Objective analysis parameters are $a = 50$ km and $b = 60$ km. Contour interval is equivalent to 2 dyn. cm.

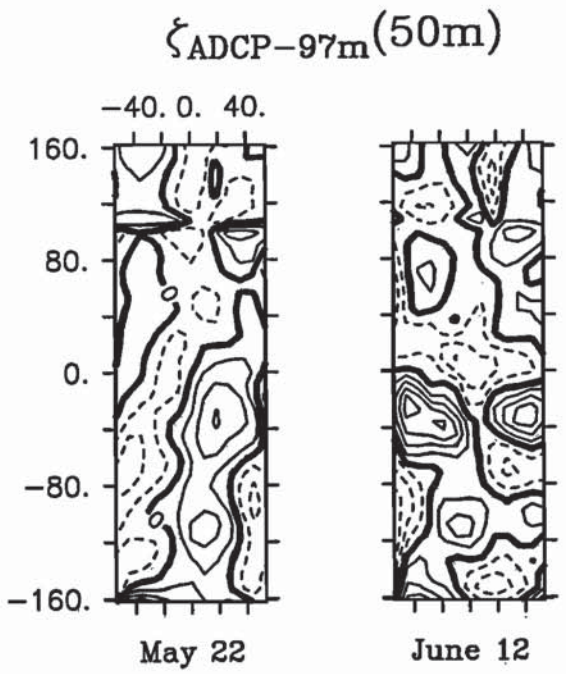

Fig. 8. Relative vorticity ζ at 50 m depth from the absolute stream function analyses based on ADCP data at 97 m for May 22 and June 12, 1987. Objective analysis parameters are $a = 50$ km and $b = 60$ km. Contour interval is 0.1 f_0 and max $|\zeta| = 0.45 f_0$.

while the ADCP analysis indicates a strong eddy (10 dyn. cm). The eddy west of the jet in the southern portion of the domain is similar in the two fields, although the ADCP stream function indicates a somewhat stronger eddy than does the LNM analysis.

The most significant discrepancy between the two analyses (Figures 6 and 7) lies in the southeast quadrant of the model domain, where the LNM analysis indicates a southward meandering flow. The ADCP stream function indicates northward flow on the inshore edge of the domain. This northward flow splits about 90 km south of the center of our domain, with roughly half of the flow turning to the south and merging with the jet, while the other half continues northward 90 km before also turning south and combining with the jet. These streamlines compare very well with those inferred from the drifter tracks of *Paduan and Niiler* [1990]. These drifters were deployed May 18–20, along the southeastern edge of the model domain, near 38.1°N, 123.6°W. They followed both the northern and southern paths of this flow and indicated the anticyclonic meander located off Point Arena. The flow implied by the drifter tracks is opposite to that of the LNM analysis. One drifter was caught in the closed circulation to the north for a single rotation. The drifters which followed the northern path around the eddy indicate a path parallel to the jet streamlines of the ADCP analysis, yet crossing four streamlines of the LNM analysis before exiting the domain. This agreement with independent data strongly supports use of ADCP measurements to produce the absolute stream function in the coastal transition zone.

By using a statistical measure of the difference between the ADCP and LNM based stream function fields, the dependence of these differences upon correlation function parameters and the particular LNM may be evaluated. Two statistical measures are used to assess the difference of two sets of fields whether comparing analysis with analysis or model solution with analysis. The first is the normalized variance of the difference,

$$\mathrm{nvd}\,(\psi, \psi_r, z) = \frac{\sum\left(\left(\psi - \tilde{\psi}\right) - \left(\psi_r - \tilde{\psi}_r\right)\right)^2}{\sum\left(\psi_r - \tilde{\psi}_r\right)^2}, \tag{10}$$

and the second is the correlation,

$$\mathrm{cor}\,(\psi, \psi_r, z) = \frac{\sum\left(\left(\psi - \tilde{\psi}\right)\left(\psi_r - \tilde{\psi}_r\right)\right)}{\sqrt{\sum\left(\psi - \tilde{\psi}\right)^2 \sum\left(\psi_r - \tilde{\psi}_r\right)^2}}, \tag{11}$$

where the summation is carried out over all model grid points and ψ_r is the reference stream function. The reference stream function is always a 97-m-ADCP-based analysis stream function, while ψ is either an analysis or model stream function. The reference stream function is always created with the same correlation parameters used to produce ψ when ψ is an analysis stream function. If ψ is a model solution, then the correlation parameters are those used to determine the boundary and initial conditions. Since observed data are available only in the upper 500 m, we will restrict our attention to this region. The 150-m level, which is in the main thermocline, and the integrated values, $1/500\ \mathrm{m} \int_{500\ \mathrm{m}}^{0\ \mathrm{m}} dz$, generally will be reported. The depth-integrated nvd and cor will be represented by invd and icor respectively. While the basic form of cor and nvd are similar,

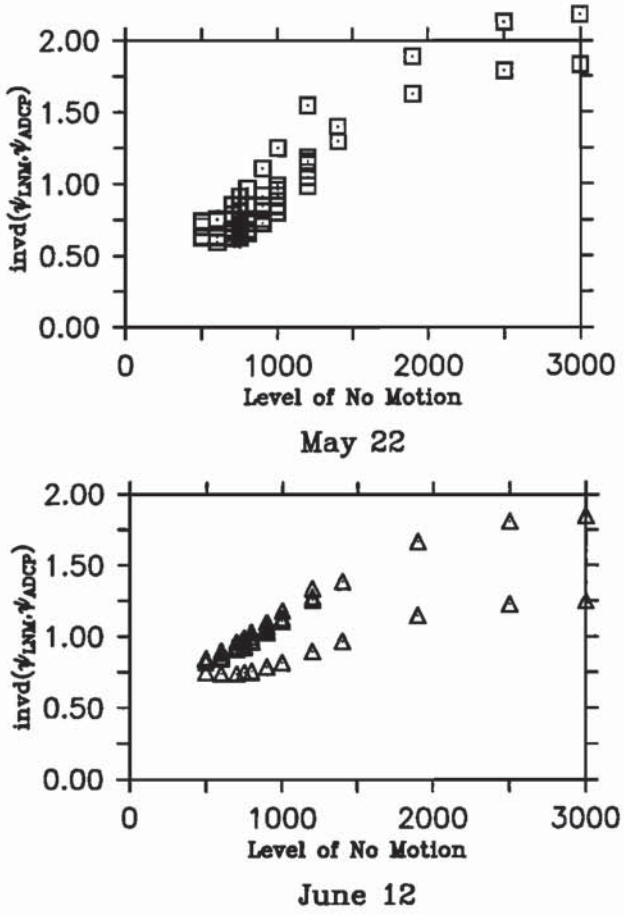

Fig. 9. Depth-integrated normalized variance of the difference between the LNM analyses and the 97-m ADCP analyses for May 22 (diamonds) and June 12 (triangles). All objective analysis parameter sets were used at each level of no motion; therefore there are six values for each level of no motion. The ADCP analysis used for comparison with a particular LNM analysis is that which has the same OA parameters.

each responds differently to difference fields. The nvd is more sensitive to variations in magnitude of the fields and cor indicates variations in the overall pattern of the fields.

The invd of each LNM analysis from the 97-m-ADCP analysis with the same correlation parameters is shown in Figure 9 for all of the correlation parameter choices (Table 2) and levels of no motion. This figure indicates that a level of no motion of 600–700 m produces the best agreement between the LNM and ADCP analyses. Changes in correlation parameters produce a wide variation; yet the general trend is consistent: very high values of invd for deep levels of no motion and a slight minimum invd of 0.6 for analyses with a 600 m level of no motion.

3. ASSIMILATION EXPERIMENTS

Assimilation experiments are conducted to develop an understanding of the relationship of the parameters used for statistical analysis, subgrid-scale processes, and numerical integration of the QG equations. The objective is to develop the solution in best agreement with the data. Assimilation experiments with LNM-based initial and boundary conditions will be considered first, with an emphasis on the influence of the particular LNM. Experiments with ADCP-based initial and boundary conditions will be considered second, examining the effect of correlation parameter choice, the influence of topography, and the variation between solutions forced with ADCP data from different depths. The solution in best agreement with the June 12 data will emerge from this analysis.

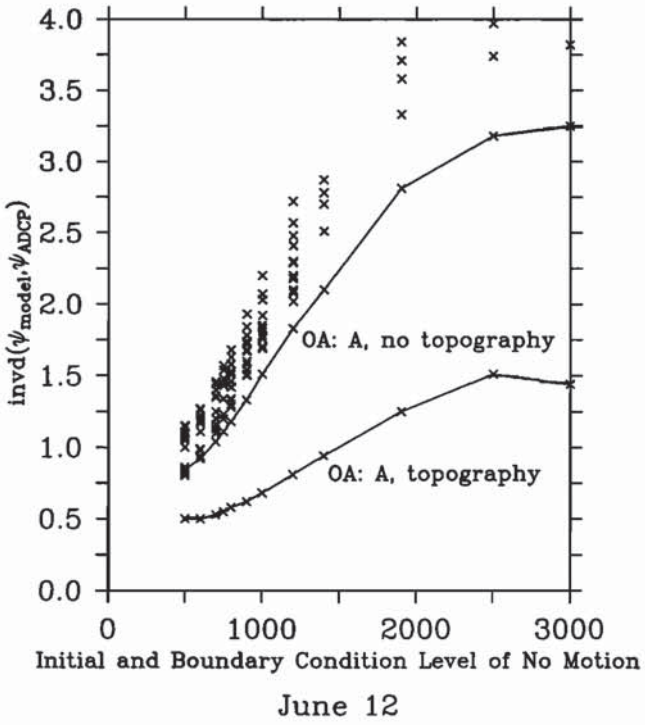

Fig. 10. Depth-integrated nvd of model solutions with level-of-no-motion initial and boundary conditions from the ADCP analyses for June 12. The set of solutions with OA parameter set A and topographic forcing and the set with OA parameter set A without topographic forcing are identified by curves. (Compare with Figure 9).

Level-of-No-Motion Studies

Assimilation modeling with data sets that do not include directly determined velocities are forced to rely upon an assumption about the absolute stream function field to convert the relative stream functions obtained from objective analysis of hydrographic data into absolute stream function for initial and boundary conditions. In the absence of information about the deep flow, the model solution which agrees best with the corresponding LNM analysis indicates the appropriate level of no motion. The Ocean Prediction Through Observation, Modeling, and Analysis (OPTOMA) program was slightly farther offshore and made use of LNM analyses in this manner [*Rienecker et al.*, 1987]. The field estimates of LNM-based assimilations have not been compared with absolute stream function fields in previous applications.

All of the LNM analyses were used as initial and boundary conditions for a series of model solutions exploring the effect of varying model parameters. Numerical and subgrid-scale parameter space was explored in 150 solutions. All solutions used parameter set I, II, or III, level i, and grid i. The correlation parameters were selected from each of the OA parameter sets indicated in Table 2, and the levels of no motion were 500, 600, 700, 750, 800, 900, 1000, 1200, 1400, 1900, 2500, and 3000 m depth. This approach is identical to that used for the OPTOMA program to determine the best LNM, except that the OPTOMA measurements included no absolute velocity measurements. The best OPTOMA LNM was determined by comparing a series of model solutions with LNM initial and boundary conditions to the final data set analysis with the same LNM. The LNM which realized the lowest difference was then selected as the best LNM [*Rienecker et al.*, 1987]. In this study, we have the ADCP analyses with which to compare.

The invd of the LNM-based solution and the June 12 97-m-ADCP analysis created with the same correlation parameter set is shown in Figure 10. These should be compared with the invd for the initial conditions, which are the LNM analyses for May 22, and with the invd for the LNM analyses for June 12 (Figure 9). There is a clear distinction between one set of solutions and all of the others. The OA correlation parameter set A ($a = 50$ km, $b = 60$ km) and inclusion of topographic forcing produces the best set of solutions. The flat-bottom, OA parameter set A solutions are also indicated by a curve. The OA parameter set A, flat-bottom solutions produce the second best set of solutions. Several other individual solutions which are slightly better or slightly worse than the flat-bottom results at the 500 m LNM are the other OA parameter set solutions (B–F) with topographic forcing. This suggests that OA parameter set A and topographic forcing comparably improve model solutions. The significant result of these LNM studies is that including dynamics has improved the quality of the data by reducing the invd from 0.74 to 0.50 for a 600 m LNM using an initial condition which began with an invd of 0.60. Hence dynamics provides more than a constrained interpolation; the combination of dynamics and data provides an improved field estimate for June 12.

ADCP-Based Studies

A series of experiments was conducted to determine the effect of analysis, numerical, and subgrid-scale parameters and to find the best solution using the ADCP data to make the stream function fields absolute. One of the parameters varied was the ADCP-data depth. To understand the significance of variations in model solutions with different ADCP-based initial and boundary conditions, the ADCP-based analyses were intercompared. The invd of the 121-m-ADCP-based analysis from the 97-m-ADCP-based analysis is 0.03, and the invd of the 146-m-ADCP-based

analysis from 97-m-ADCP-based analysis is 0.05. The relatively small difference between analyses with different ADCP data levels should not be interpreted to mean that the errors in the ADCP measurements are small, since absolute velocity estimates at separate levels are not independent. For example, the ship velocity estimates are common to the three velocity levels and may be a significant error source. The differences between analyses using the three ADCP data sets are systematic; the jet becomes weaker at all depths as the ADCP data depth increases. This indicates that the shear in the jet velocity, as measured by the ADCP, is stronger than the geostrophic velocity shear implied by the hydrographic measurements.

The choice of ADCP data level was also significant in determining the solution. Figure 11 presents the best results for each ADCP level from all of the ADCP analysis based solutions. With topographic forcing, there is a relatively small variation between model solutions. With or without topographic forcing, there is very little difference between the solutions using 121-m ADCP data and those using 146-m data. The 97-m-ADCP-based solution without topographic forcing compares to the June 12 analysis significantly better than all of the other solutions compare to the June 12 analysis. This result, combined with the earlier observation that the jet is stronger when shallower ADCP data depths are used, indicates that the strongest jet is needed to provide the best available solution. The best solution uses correlation parameter set A, parameter set III, level i, grid i, a 16-1-1 filter, and a flat bottom. This solution will appear in the following intercomparisons and will be analyzed to understand the kinematics and dynamics.

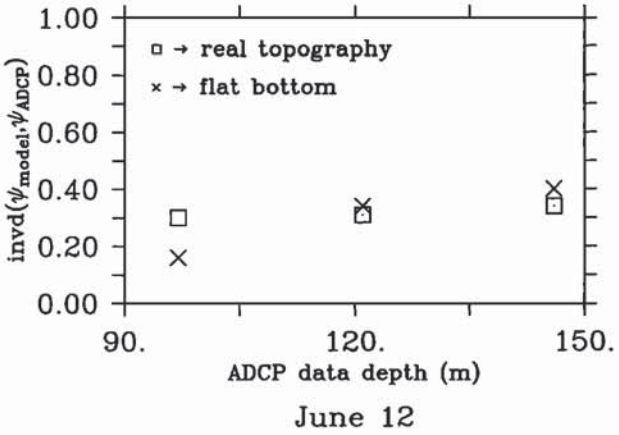

Fig. 11. Comparison of best model solutions using each ADCP data level, with and without topographic forcing to the corresponding ADCP analyses for June 12.

We next consider the effect of the OA parameters and of including or excluding topography. All solutions used in this analysis are based upon model parameter set III, grid i, and level i with a 16-1-1 filter; only the objective analysis parameters and whether or not topography was included were varied between solutions. Figure 12 shows the invd versus the decay length scale a and the zero crossing b. The combination a=50 km, b=60 km, which is OA parameter set A, results in the lowest invd both with and without topographic forcing. This is consistent with the LNM result except that the best solution is without topographic forcing. Comparing solutions with and without topographic forcing, the topographically forced solutions are better than their unforced counterparts except in the best case. Topography is a controlling

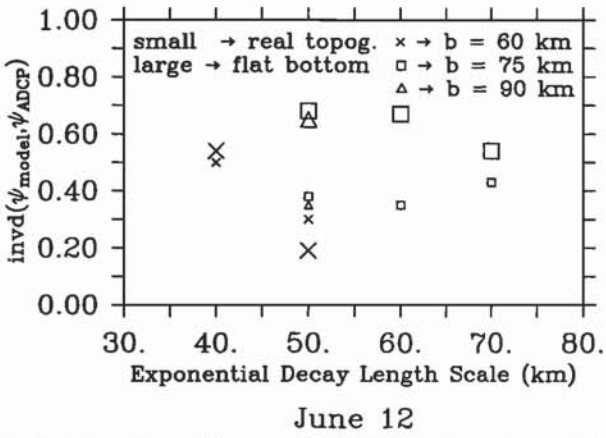

Fig. 12. Comparison of best model solutions using each correlation parameter set, with and without topographic forcing to the corresponding ADCP analyses for June 12.

factor, generally reducing the difference between analysis and solution up to the limits of the data set, which lacks deep flow measurements. Given the steep topography on the edge of the domain, how can a topography-free case give the best results? There are two important considerations. First, deep-ocean flows are expected to be in near balance with the local topography; flow is generally along fH^{-1} contours. As a result, the instantaneous dynamic effect of the topography may be small because the initial and boundary conditions are in near balance with the topography and the effect of topography is not missed over the relatively short integration period of 3 weeks. Second, the inshore model boundary was placed along the steepest bottom topography. The effect of topographic forcing is expected to be largest on this edge, and the boundary conditions will have this effect included, thereby providing the most significant topographic-forcing effects through boundary conditions. If deep ocean data were available to specify the deep currents directly, then a better solution with topographic forcing included would be expected. Experimentation with the method of stream function extrapolation to the deep ocean resulted in no improvement in the agreement between model solution and data analysis for June 12. The combination of a careful positioning of the model domain and an absence of strong direct topographic effects at the main thermocline appears to result in satisfactory model solutions without topographic forcing. Another possibility is that solutions with topography violate the quasi-geostrophic assumptions, which leads to a final solution that compares relatively poorly with the final analysis.

A range of numerical parameter choices was used with varying analysis and subgrid-scale parameters. As was noted in previous studies [*Walstad and Robinson*, 1990], once the time step is sufficiently small, further reasonable reductions do not affect the solutions. Also considered were increases in the horizontal and vertical resolution of the model; neither of these improved the results. This is consistent with the findings of *Haidvogel et al.* [1980]; given sufficient resolution, their solutions exhibited little kinetic energy variation in a large regional mesoscale eddy field simulation.

In an attempt to understand the importance of dynamics in determining the final solution, the parameters α and β in equation (1a) were varied and filtering was eliminated. Setting $\alpha = 0$ and otherwise repeating the best solution, which is equivalent to removing the nonlinearity, resulted in an increase of the invd from 0.16 to 0.26. Setting $\beta = 0$ had little effect, increasing the invd to 0.18. With $\alpha = \beta = 0$, the invd was 0.26.

Eliminating the filter with $\alpha = \beta = 0$ resulted in a slight increase to 0.27. Note that there is still a dynamic contribution by the boundaries through partitioning of vorticity into relative and stretching components (eqn. 1b). The May 22 and June 12 97-m-ADCP analyses have an invd of 0.54. Nonlinear vorticity dynamics is apparently responsible for roughly 30% of the change during this 3-week period (since the best invd is 0.16, the $\alpha = 0$ and no-filtering invd is 0.27, and the no-dynamics invd is 0.54; $(0.27 - 0.16)/(0.54 - 0.16) = 0.11/0.38 \approx 0.29$). The solution in this model domain during this time period is controlled both by the local process of vorticity advection (eqn. (1a)) and the boundary value problem which partitions vorticity into relative and stretching components (eqn. (1b)). The best solution is considerably better than a solution neglecting the horizontal transport of vorticity.

Since the boundary conditions are linear interpolations between the initial and final data sets, the boundary forcing varies slowly although the advective speeds are quite high. Typical jet speeds are 30 cm s^{-1}, which rapidly draws boundary vorticity into the interior and removes the vorticity of the initial condition. A reasonable expectation would be that the flow would initially change rapidly as boundary vorticity is advected into the region; then the flow would change monotonically toward the final solution. This speculation was examined by comparing the best model solution for each day with a linear interpolation between the May 22 and June 12 analyses. The daily invd of the model solution and the linear interpolation of the analyses is seen in Figure 13. The initial divergence of the solution from the linear interpolation is slow, reaching a maximum after about 5 days. Solution and linear interpolation continue to diverge through May 31. During the next 5 days, the difference remains relatively constant with an invd of 0.42, then on June 5 the model solution and the linear interpolation begin to converge. During the next 7 days the invd is reduced from a high of 0.42 to 0.16. This behavior is substantially different from the gradual changes in the boundary conditions and suggests that interior dynamical processes are important to the evolution of the solution.

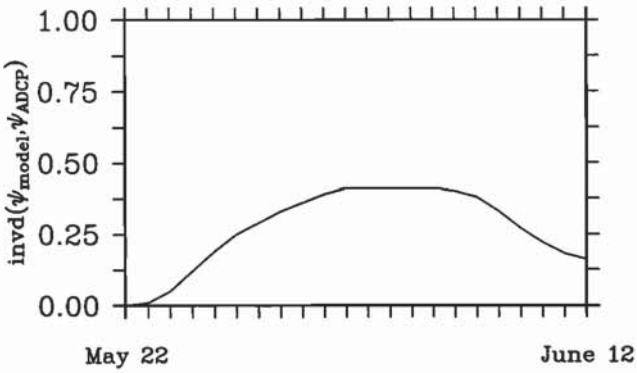

Fig. 13. Depth-integrated nvd of the best model solution from a linear interpolation between the May 22 and June 12 analyses.

An independent data set, consisting of three cross-jet sections, was collected along 125°W on June 3, 4, and 5 [*Dewey and Moum*, 1990]. These sections overlie the assimilation region as indicated in Figure 14. ADCP measurements are one component of the independent data set; the eastward velocity is shown in Figure 15. The model eastward velocity along this section on June 1, 3–5, and 7 is shown in Figure 16. The behavior of the observed jet is reproduced by the model solution in two key aspects, jet

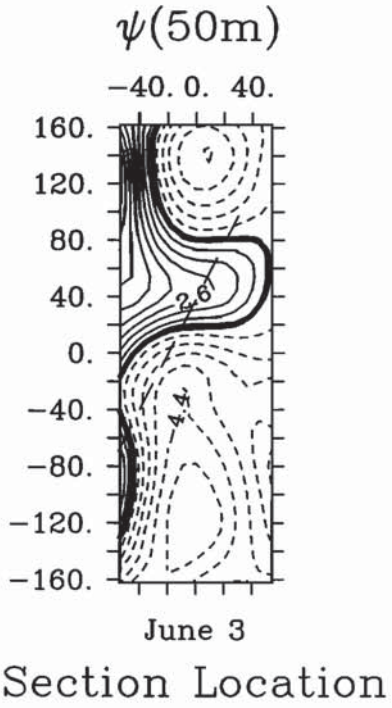

Fig. 14. Location of the sections described by *Dewey and Moum* [1990] (dashed line) with respect to the model domain. The field is the June 3 50-m stream function with a contour interval equivalent to 2 dyn. cm.

strengthening and southward movement. The strengthening is slightly weaker in the model; velocities increase from 40 cm s^{-1} to 60 cm s^{-1}, whereas the measured velocities reach a peak of 80 cm s^{-1}. We note that the velocities presented by *Dewey and Moum* [1990] were filtered over length scales of about 1.5 km, which is far less than the mesoscale for which quasi-geostrophy is intended. In addition, *Dewey and Moum* [1990] note that some of this strengthening may be due to vertical mixing and also that the winds varied rapidly at this time from weak southerly flow on June 3 to strong northerly flow on June 5, which would enhance the mixed layer (20–40 m depth) velocities in the jet. The data indicates that the region with speeds in excess of of 80 cm s^{-1} is very narrow (10 km) and confined to the upper 20 m. Southward movement of the jet in the model solution begins on June 1 with the jet at 39.05°N. By June 7, the jet reaches 38.75. This independent verification of the jet position and behavior at the midpoint of the solution period supports our contention that the model solution is very similar to the ocean during the period May 22 to June 12, 1987. An interesting observation is that the solution and independent data agree at the time when the solution is most different from a linear interpolation (Figure 13). Certainly, there are substantial limitations. We are forced to treat the data as synoptic and to extrapolate to obtain the deep fields; yet the model solution is reproducing the observed behavior of the jet, strongly suggesting that we have captured the fundamental dynamics of the jet.

4. PHYSICAL ANALYSIS

A primary advantage of assimilation modeling is that it provides a dynamically constrained interpolation between surveys. If the final solution agrees with the analyses, these fields are much more than a linear or statistical interpolation. In the best case, the solution and analysis for June 12 agree very well, having an invd of 0.16 and correlation of 0.93. Agreement with independent

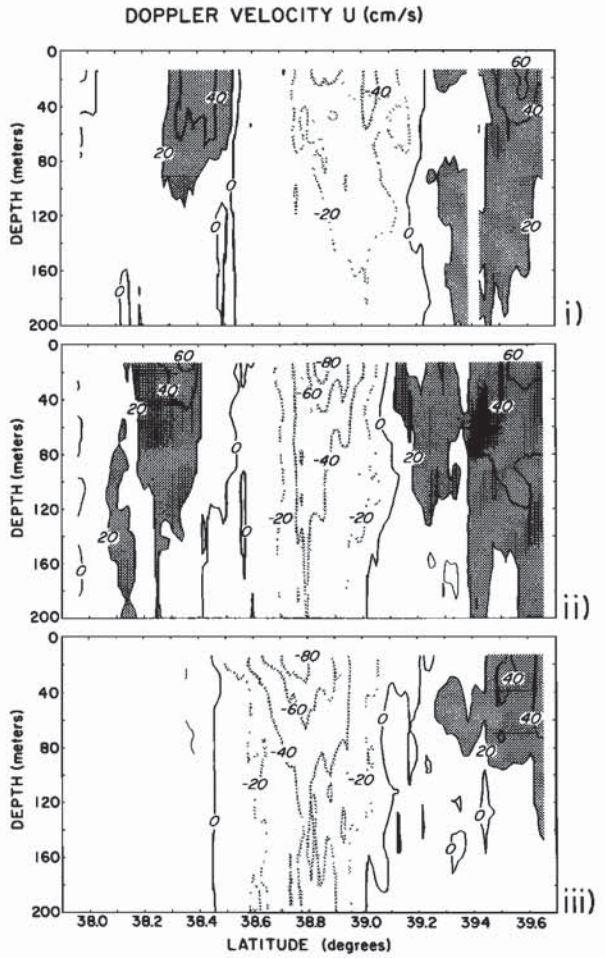

Fig. 15. Velocity sections, surface to 200 m, from three ADCP sections i, ii, and iii made June 3, 4, and 5, respectively, from *Dewey and Moum* [1990]. The section location is indicated in Figure 14. Velocity contours are 20 cm s^{-1}; dashed contours indicate negative (westward) flow.

data prior to the final solution further suggests that the fields are evolving in a manner quite similar to the real ocean. Given this very good agreement, the kinematics and dynamics of the model fields produced by the best case, with model parameters III, grid i, level i, a 16-1-1 filter, OA parameter set A, and no topography, are regarded as representative of the CTZ between May 22 and June 12, 1987, and are utilized for further analysis.

Kinematics

The initial flow at 50 m, as seen in Figure 17a, consists of (1) a southward jet entering the domain at the northwest corner, (2) a cyclonic eddy to the north, (3) two jet meanders on the western edge of the domain, and (4) a northward flow on the southeastern edge of the domain. Similar, but weaker, features are seen at the other thermocline levels. The apparent jet meanders on the western edge of the domain actually may be eddies, since the the offshore information needed to identify these features is not available. However, the absence of a sea surface temperature signal from the IR imagery [*Kosro et al.*, this issue] and subsequent behavior of these flow features (see below) strongly suggest that they are components of the jet. The northern eddy is identifiable from data north of the region [*Kosro et al.*, this issue]; ADCP measurements (Figure 3) indicate that the northern eddy recirculates. As the jet enters the domain, one third of the

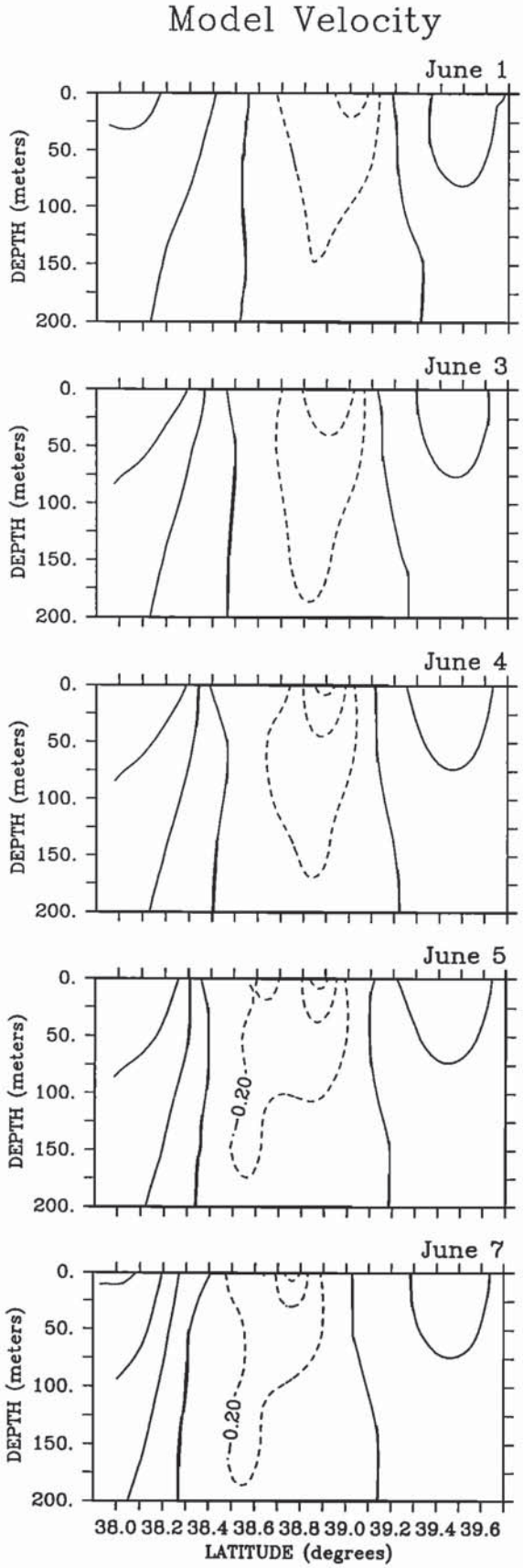

Fig. 16. Velocity sections, surface to 200 m, for June 1, 3, 4, 5, and 7 from the best model solution. The section location is indicated in Figure 14. Velocity contours are 20 cm s^{-1}; dashed contours indicate negative (westward) flow.

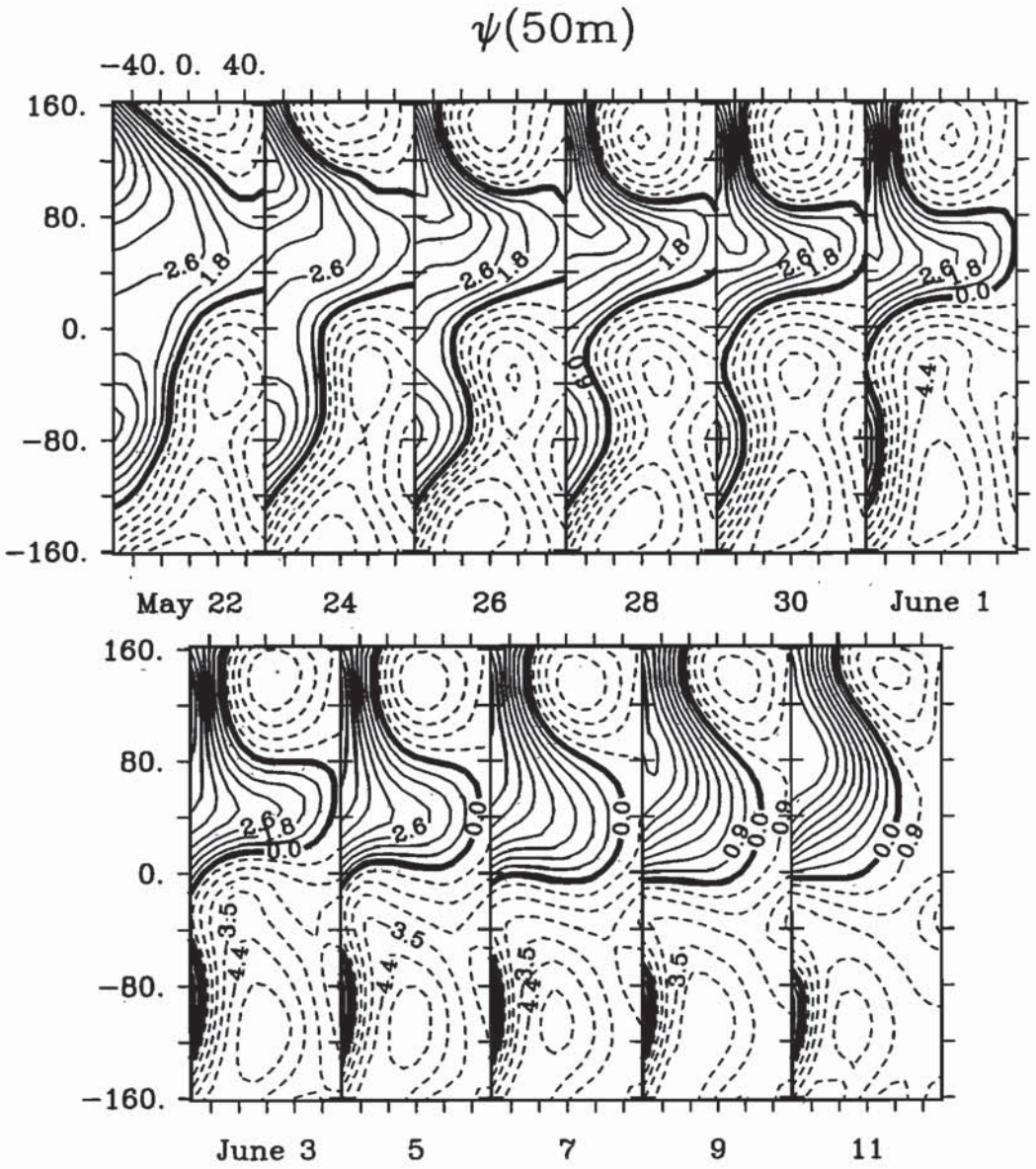

Fig. 17. (a) Maps of stream function at 50 m depth every other day from the best solution. Contour interval is equivalent to 2 dyn. cm.

flow turns to the north in the northern eddy, and nearly one half of the flow turns to the west, meandering outside of the domain. The remaining sixth continues to the south, combining with the southward continuation of the northward flow and the southern jet meander. Northward flow in the southeast quadrant along the southern portion of the inshore edge of the domain turns to the south in two locations, off Point Reyes and off Point Arena. These two southward continuations combine with the southern jet meander and the flow from the north to exit the domain as a jet in the southwest corner. This jet is slightly slower and broader than the entering jet yet carries a greater volume in the upper 500 m after combining with the southward extension of the inshore flow.

On May 24 the northern jet has extended farther into the region, while the southern jet has meandered. This trend continues through May 26. The meanders at the offshore edge of the domain now clearly appear to be part of the jet, although the northern feature may include some recirculation. Also, the eddy formed by the northward flow as it turns to the south has strengthened after weakening for the first 2 days. By May 28 the northern and southern portions of the jet are strongly connected within the study area. A sharp meander in the jet has developed between these two portions. The southern portion of the jet has begun to move offshore.

A continuing strong flow from the north to south is seen on June 1. The closed eddy has disappeared from the center of the domain, and the southern portion of the jet is meandering farther offshore. The northern eddy has entered farther into the domain and strengthened, with the jet flowing nearly parallel to the edge of the domain for 80 km. During the next few days, the sharp shoreward meander of the jet relaxes. This process continues and the northern eddy weakens until the end of the integration period, June 12.

The final field on June 12 (Figure 17b) indicates a jet that enters the domain at the western end of the northern edge and travels southeastward for 80 km before turning offshore. Cold water is being drawn off the coast on the southern portion of the offshore

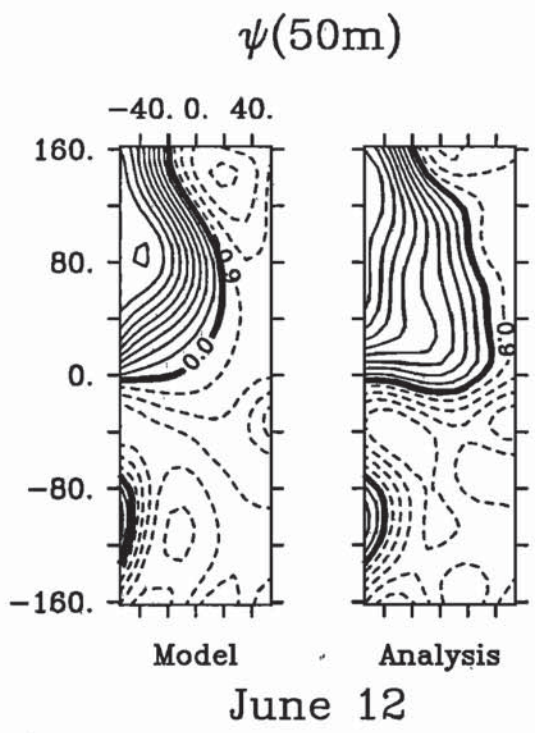

Fig. 17. (b) Model and analysis 50-m stream function on June 12. Contour interval is equivalent to 2 dyn. cm.

meander. Farther to the south, the jet meanders back through the offshore edge of the domain. Northward flow has weakened leaving behind a small cyclonic eddy west of Point Reyes.

Dynamics

Dynamically, the region may be divided into four parts; meandering jet in the southwestern portion of the domain, inflow jet in the northwestern corner, northern cyclonic eddy in the northeastern corner, and the northward current in the southeastern quadrant. Each feature has a unique signature in the energy balances, some of which may be identified with the dynamics of idealized flows. As would be expected in a turbulent flow, structures are not easily characterized by simple flows; they can not be readily identified as baroclinic instability, barotropic instability, or jet meandering. Rather, the important energy terms will be identified and contrasted with idealized studies.

The dynamics of the flow will be evaluated using maps of energy balance terms calculated from the best model solution. The kinetic and available potential energy equations and their symbolic representations as introduced by *Pinardi and Robinson* [1986] and described in Table 3 are

$$\begin{aligned} K_t =& -\alpha\nabla\cdot(\mathbf{u}K) \\ & - \nabla\cdot\left(\psi\left(\hat{k}\times\mathbf{u}_t + \alpha\mathbf{u}\cdot\nabla\left(\hat{k}\times\mathbf{u}\right) - \beta y\mathbf{u}\right)\right) \\ & - \frac{\partial}{\partial z}(\psi w_1) + \psi_z w_1 + \text{ filter effect on } K, \\ =& \Delta F_K + \Delta F_\pi + \delta f_\pi - b + B_K, \\ A_t =& -\alpha\nabla\cdot(\mathbf{u}A) - \psi_z w_1 + \text{ filter effect on A}, \\ =& \Delta F_A + b + B_A, \end{aligned} \tag{12}$$

TABLE 3. Symbolic Representation and Description of Energy Equation Terms

Energy Equation Term	Description
K	kinetic energy, $\frac{1}{2}(u^2+v^2)$.
A	available potential energy, $\frac{1}{2}\sigma\Gamma^2(\psi_z^2)$.
K_t	time rate of change of kinetic energy.
ΔF_K	divergence in the advection of kinetic energy.
$DK/Dt = K_t - \Delta F_K$	time rate of change of kinetic energy following fluid parcels.
ΔF_π	horizontal pressure work divergence.
δf_π	vertical pressure work divergence.
$\Delta_3 F_\pi = \Delta F_\pi + \delta f_\pi$	total pressure work divergence.
b	buoyancy work.
B_K	kinetic energy filter effects.
A_t	time rate of change of available potential energy.
ΔF_A	divergence in the advection of available potential energy.
B_A	available potential energy filter effects.

with

$$\begin{aligned} \Delta F_K &= -\alpha\nabla\cdot(\mathbf{u}K), \\ \Delta F_\pi &= -\nabla\cdot\left(\psi\left(\hat{k}\times\mathbf{u}_t + \alpha\mathbf{u}\cdot\nabla\left(\hat{k}\times\mathbf{u}\right) - \beta y\mathbf{u}\right)\right), \\ \delta f_\pi &= -\frac{\partial}{\partial z}(\psi w_1), \qquad B_K = \text{ filter effect on } K, \\ b &= -\psi_z w_1, \\ \Delta F_A &= -\alpha\nabla\cdot(\mathbf{u}A), \qquad B_A = \text{ filter effect on } A, \end{aligned}$$

where the horizontal velocities are the lowest-order terms in a Rossby number expansion and the vertical velocity is a first-order term: $\mathbf{u} = (u_0, v_0)$, $u_0 = -\psi_y$, $v_0 = \psi_x$, and $w = \epsilon w_1$. The terms in the symbolic representation correspond in order to those in the corresponding equation, except the filter effects which are not easily represented by operators in the kinetic and available gravitational energy equations. Note that the calculations are made neglecting two grid points on each side of the domain. Since the solution has 9-km resolution, the analysis domain is 72 by 288 km. We use a methodology similar to that of *Pinardi and Robinson* [1986] but constructed such that the energy analysis algorithm includes horizontal finite element, vertical finite difference, and Adams-Bashforth time difference operators consistent with the model numerical operators.

The meandering jet is seen in the May 23 50-m kinetic energy distribution as a ridge which extends from the center of the region to the southwest corner (Figure 18). In this region of the domain, the jet is identifiable as a ridge of kinetic energy K at each depth to 500 m but gradually weakening with increasing depth. The K maps for May 23 to June 10 indicate the meandering and offshore movement of the jet previously identified from stream function

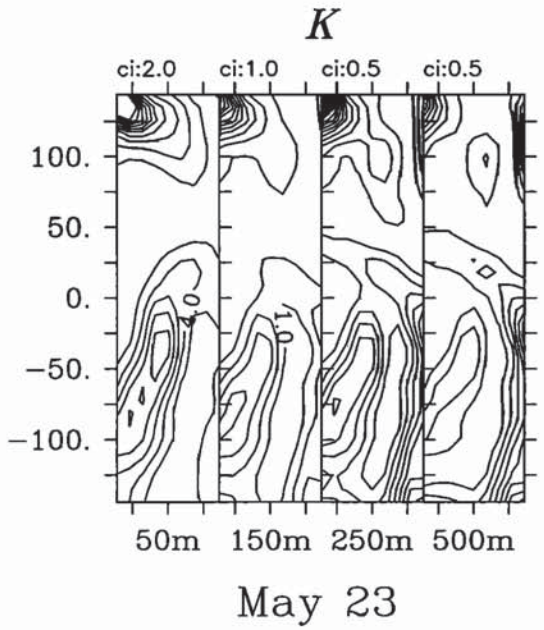

Fig. 18. Kinetic energy maps at 50, 150, 250, and 500 m depth on May 23, 1987 from the 97-m ADCP, OA parameter set A analysis.

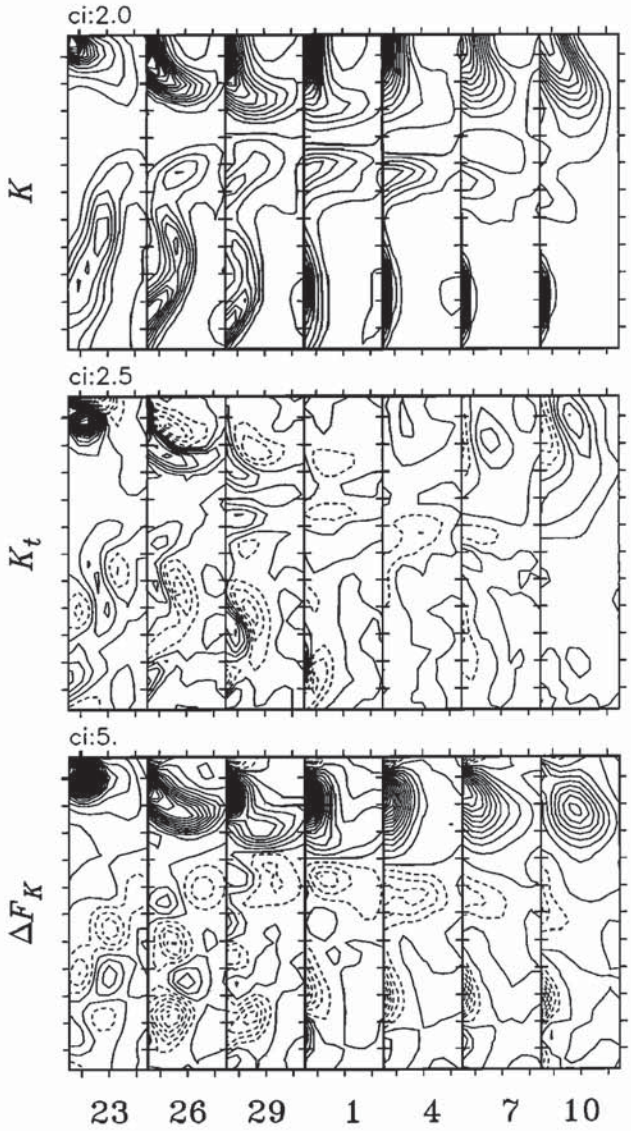

Fig. 19. Kinetic energy (K), time rate of change of kinetic energy (K_t), and divergence of horizontal advection of kinetic energy (ΔF_K) at 50 m depth in a 72 by 288 km region every 3 days for May 23 through June 10. Dashed contours indicate negative values. Axis tick marks are at 25 km intervals.

(Figure 19). On May 23 the jet, as indicated by kinetic energy, was nearly straight. By May 26 a significant meander of wavelength 130–150 km had developed. This meander development continued through May 29, but the meander was also moving to the west-southwest. The K_t (time rate of change in K) term is a good indicator of the direction of movement of a jet. The pattern of highs and lows is consistent with meander growth, positive on the outside of developing meanders and negative on the inside. Meander propagation would exhibit increasing kinetic energy on the leading edge of the meanders and decreasing kinetic energy on the trailing edge. To assess the dynamics causing this behavior, we examine the individual kinetic energy equation terms. This will be done for each of the features noted in the kinematics. We consider first the jet meander in the southwestern quadrant, then the inflow jet in the northwestern corner, the eddy to the northeast, and finally the northern flow in the southeastern quadrant.

Note the pattern of highs and lows in the divergence of horizontal advection of kinetic energy, ΔF_K, on May 23 as compared with the highs and lows in K_t. In the vicinity of the jet, the local maxima and minima in ΔF_K were approximately coincident with the local maxima and minima of K_t as seen in Figure 19. This indicates that the divergence of kinetic energy advection was a mechanism forcing the jet meander. An exception is the region just west of the center of the domain, where K was increasing, yet ΔF_K was negative. Total pressure work divergence, $\Delta_3 F_\pi$, and buoyancy work, $-b$, were contributing positively in this region (Figures 20 and 21). Total pressure work divergence nearly balanced the time rate of change of kinetic energy following water parcels, DK/Dt, as is indicated in Figure 21. It did not achieve this balance just west of the center of the region at the northern end of the meandering portion of the jet. There the buoyancy work was significantly contributing to the kinetic energy. Overall, the divergence of horizontal advection of kinetic energy was primarily forcing the jet meander, with pressure work redistributing energy horizontally and vertically while the total pressure work divergence was nearly in balance with the time rate of change of kinetic energy following water parcels. Buoyancy work was contributing to meander growth at the northern meander and reducing the growth of the southern meander.

By May 26 the situation had changed: K_t was negative on the outside edge of the anticyclonic meander, though the K_t maximum is located north of this meander. The ΔF_K pattern remained consistent with meander growth, positive on the outside of the meander and negative on the inside. While horizontal pressure work was removing energy in a small region adjacent to the meander, vertical pressure work was acting in a larger region and their combination was significantly removing energy (Figures 20 and 21). Buoyancy work, $-b$, was contributing to the loss of kinetic energy. Meander growth had ended; advection of kinetic energy continued to support meander growth, but pressure work was redistributing kinetic energy to other parts of the flow at a greater rate.

The along-jet length scale of the horizontal processes ΔF_K and ΔF_π was approximately 65 km, while the vertical processes δf_π and b were dominated by the 100-km along-jet length scale in the

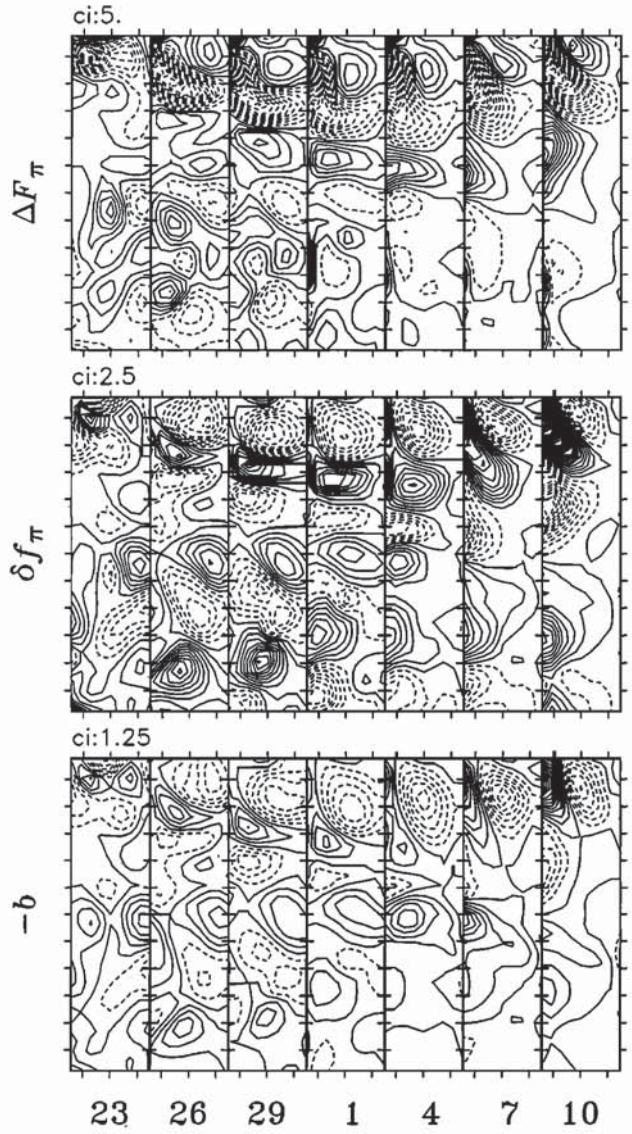

Fig. 20. Divergence of horizontal pressure work (ΔF_π), divergence of vertical pressure work (δf_π), and buoyancy work ($-b$) at 50 m depth in a 72 by 288 km region every 3 days for May 23 through June 10. Axis tick marks are at 25 km intervals.

vicinity of the meandering jet. Note that the length scale of the terms in the energy balances is one-half the meander wavelength as shown by *Pierce et al.* [this issue]. By May 29 the 65-km length scale in ΔF_K and ΔF_π was giving way to the 100-km length scale (Figures 19 and 20). As these scales changed, the fundamental balance also changed. Advection of kinetic energy, ΔF_K, was acting to decrease meander amplitude, contributing to the departure of this meander from the domain. Pressure work, $\Delta_3 F_\pi$, was acting to increase the meander amplitude. While both horizontal and vertical pressure work were important, vertical pressure work divergence δf_π was dominant. Early in the integration, vertical pressure work divergence is both importing and exporting energy from the first level. This changes after May 1 as the length scales increase, and by May 10 the southern quadrant is dominated by a region of positive δf_π. Buoyancy work was also acting to increase the meander amplitude as the meander departed the region.

The energy terms at the deeper levels (Figures 22, 23, and 24) exhibited similar patterns in the vicinity of the meandering jet, except that the vertical pressure work divergence was opposite in sign. The amplitude of the fields was quite different at depth, each term is comparable; buoyancy work was significant to the overall balance. The reversal of the vertical pressure work divergence indicates that energy being exported from the surface was accumulating in these upper ocean levels. By 500 m depth, the 50 m depth patterns are somewhat difficult to recognize (Figures 22 and 23). However, 500-m buoyancy work is clearly similar to 50-m buoyancy work acting on relatively large scales. This source of energy is occurring on a 100-km length scale, as is indicated by the positive region which covers most of the southwestern quadrant of the domain.

The inflow portion of the jet initially turned to the south-southeast by June 4 (Figure 19) then turned back to the east. This is reflected in the time rate of change of kinetic energy, K_t, which was positive south of the jet through May 29. Between June 1 and 4, K_t was very weak. After this, K_t became positive on

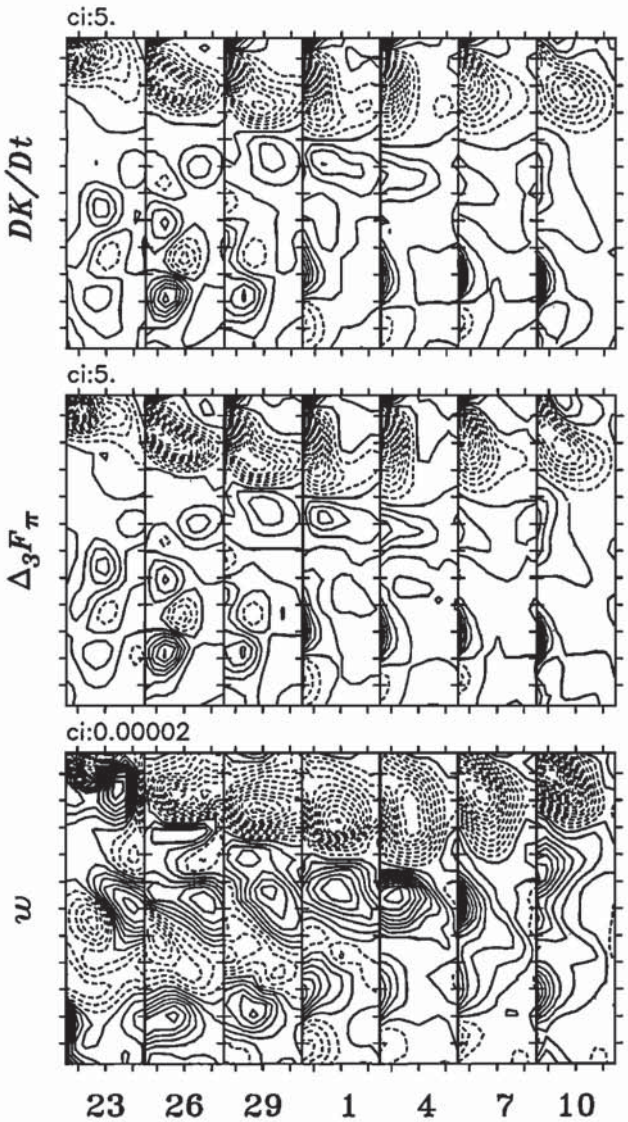

Fig. 21. Lagrangian time rate of change of kinetic energy (DK/Dt) at 50 m depth, total divergence of horizontal pressure work ($\Delta_3 F_\pi$) at 50 m depth, and vertical velocity (w) at 100 m depth in a 72 by 288 km region every 3 days for May 23 through June 10. Vertical velocity is in meters per second, 10^{-5} m s^{-1} is approximately 1 m day^{-1}. Axis tick marks are at 25 km intervals.

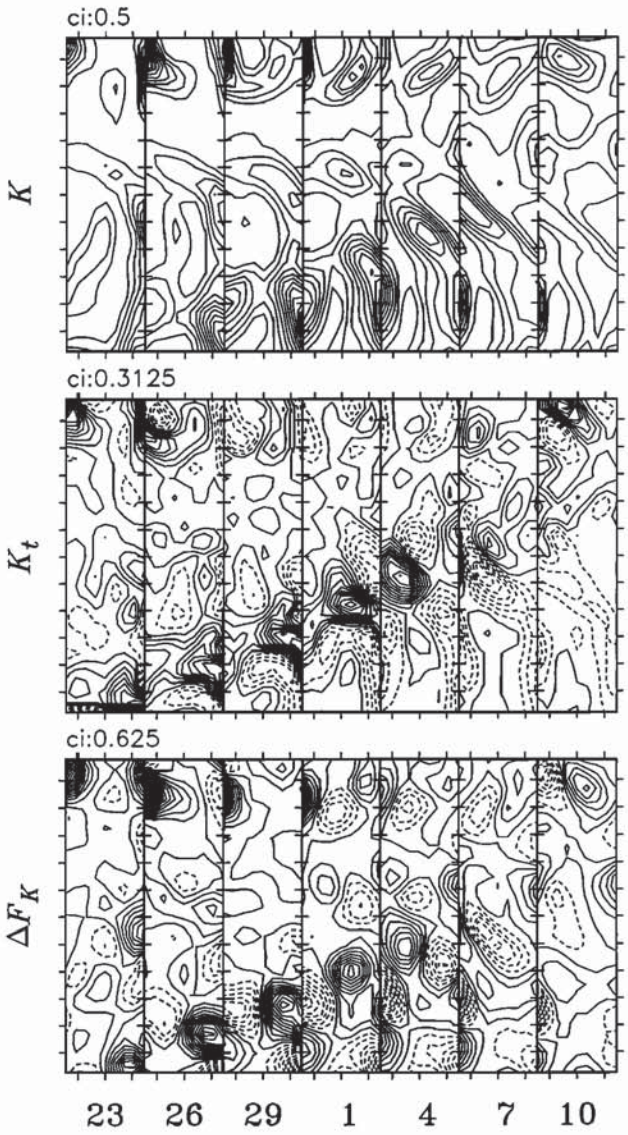

Fig. 22. Kinetic energy (K), time rate of change of kinetic energy (K_t), and divergence of horizontal advection of kinetic energy (ΔF_K) at 500 m depth in a 72 by 288 km region every 3 days for May 23 through June 10. Axis tick marks are at 25 km intervals.

the eastern edge. Throughout the experiment, ΔF_K contributed positively in the northwest corner. Until June 4 the vertical pressure work divergence was contributing to the increase in kinetic energy on the leading edge of the jet but was also removing energy on the trailing edge. Horizontal pressure work opposed the contribution of vertical pressure work. Meanwhile, buoyancy work was removing kinetic energy in the northeast corner. As the jet returned to the east, June 4–10, the $K_t = 0$ contour was primarily aligned along the y axis of the domain. This orientation is quite similar to the buoyancy work pattern, indicating that as the jet moves, kinetic energy is increasing on the leading edge and being converted to potential energy as well.

The northern flow in the southeastern quadrant of the domain at 500 m depth has a pattern of ΔF_K, ΔF_π which is quite similar to the pattern seen at 50 m in the meandering jet. The kinetic energy wedge in the southeast corner on May 26 propagated to the northwest through June 4 before beginning to leave the domain on June 7. By June 10 it was outside of the domain. As the wedge moved to the north, the positive regions of ΔF_K were coincident with regions of increasing kinetic energy. This changed on June 7, when ΔF_K was primarily removing kinetic energy. The primary change at this time was the northwestward movement of the wedge of kinetic energy under the location of the offshore flowing jet which is at 50 m depth (Figure 19).

Several parallels may be drawn between these findings, the linear stability analysis [*Pierce et al.*, this issue], and the nonlinear finite-amplitude studies [*Allen et al.*, this issue]. First, we note the robust pattern of highs and lows in ΔF_K in the meandering jet on May 23 which is contributing to the meander growth consistent with the nonlinear finite-amplitude study results. The lack of a significant buoyancy work signal with a length scale of 65–75 km (a meander wavelength of 130–150 km), combined with the linear stability analysis which indicates that the fastest growing perturbation at this wavelength was a barotropic instability, suggests that the initial meander pattern that developed during the first 6 days is primarily the result of barotropic processes. The buoyancy work and vertical pressure work divergence were primarily active on a wavelength of over 200 km. The length scale of the horizontal divergences is increasing during May

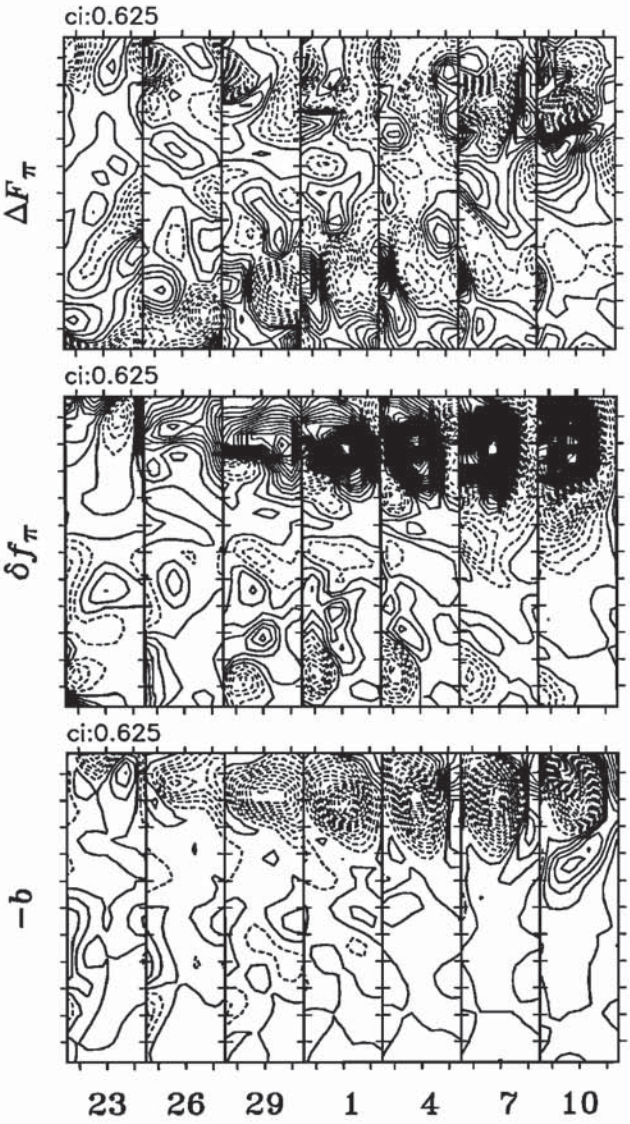

Fig. 23. Divergence of horizontal pressure work (ΔF_π), divergence of vertical pressure work (δf_π), and buoyancy work ($-b$) at 500 m depth in a 72 by 288 km region every 3 days for May 23 through June 10. Axis tick marks are at 25 km intervals.

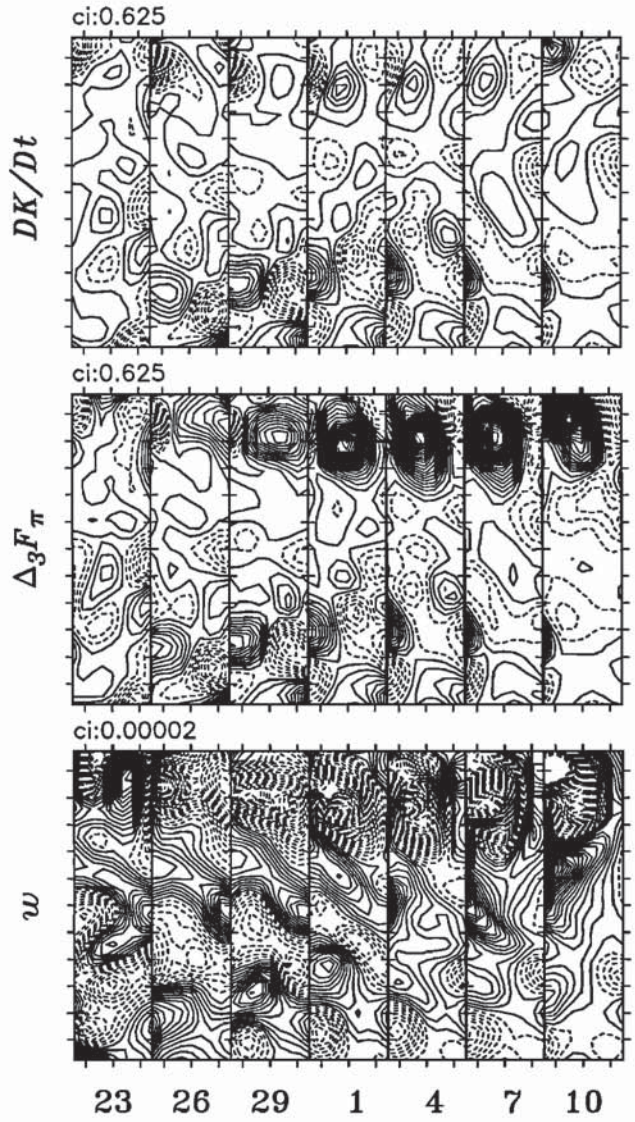

Fig. 24. Lagrangian time rate of change of kinetic energy (DK/Dt) at 500 m depth, total divergence of horizontal pressure work ($\Delta_3 F_\pi$) at 500 m depth, and vertical velocity (w) at 700 m depth in a 72 by 288 km region every 3 days for May 23 through June 10. Vertical velocity is in meters per second, 10^{-5} ms^{-1} is approximately 1 m day^{-1}. Axis tick marks are at 25 km intervals.

26 to June 4. Linear analysis and nonlinear finite-amplitude studies suggest that conversion from potential to kinetic energy should become important on these length scales. The vertical redistribution of kinetic energy through pressure work is apparent and consistent with these studies as well. Given the similarity of the amplitudes of ΔF_K and $-b$ in the vicinity of the meander below the main thermocline, baroclinic and barotropic mechanisms appear to be comparable. On the basis of these results, we conclude that a large-scale mixed instability meander is responsible for the propagation of the jet out of the southwestern corner of the domain away from the coast. The northern eddy and inflow jet experience strong conversion of kinetic to potential energy, which is consistent with the view that there is a large-scale mixed instability process that is causing the jet in the middle and southern portion of the domain to propagate offshore. This is similar to the results of *Allen et al.* [this issue], where despite a net volume-integrated conversion of potential to kinetic energy in a 250-km meander, there was a strong local conversion of kinetic to potential energy at the crest of the meander. The position, within the meander pattern, of the strong baroclinic conversion seen in the assimilation study is identical to that identified in the nonlinear finite-amplitude study.

5. DISCUSSION

Assimilation modeling of the CTZ has presented a means of estimating the dynamical processes of the region. The kinematics and dynamics of the model solution have been described and interpreted. Absolute flow measurements have provided the opportunity to assess the level-of-no-motion assumption for a flow in the neighborhood of steep topography. The effects of this assumption on the analyses and subsequent model solutions were examined.

The combination of physics and hydrographic data was found to provide a better absolute stream function estimate than was provided by the hydrographic data alone when compared with stream function made absolute by incorporation of ADCP data. This result extends those previous studies which indicated that data assimilation modeling could provide a better field estimate than objective analysis of the data located near the boundary of the model domain [*Rienecker et al.*, 1987]. It is encouraging and strengthens the argument that the dynamic interpolation between survey data is very similar to the oceanic state. It would be helpful to examine the relationship between the ability of data assimilation to improve field estimates and the quality of the data. This may be difficult with real ocean flows, since there will always be a substantial errors as long as data are collected quasi-synoptically. An alternative is to use an observing and assimilation system simulation approach so that degradation of data quality may be controlled. This would also permit analysis of the effect of initialization and boundary forcing errors on the terms in the energy balance.

The objective of this study was to obtain an understanding of the dynamics of the CTZ flow during the late spring of 1987. A quasi-geostrophic model solution was obtained that compares well with the survey data for June 12 and with independent measurements of jet sections at an intermediate time despite pressing the limits of the formal quasi-geostrophic approximation. The local energy balances of this numerical solution were calculated and analyzed. From this analysis, in conjunction with linear analysis of the stability of the jet and nonlinear finite-amplitude studies, we have identified jet meander dynamics which support the characterization of the CTZ flow field as a meandering jet which gradually propagates offshore [*Strub et al.*, this issue]. The dynamics of the northward flow and interaction of the jet with the northern eddy were described. These studies are continuing with application to the 1988 CTZ data set and application of new models and assimilation methodology.

Acknowledgments. L. J. Walstad and J. S. Allen have been supported by ONR Coastal Sciences Program grants N00014-87-K-0009 and N0014-90-J-1051. A. Huyer and P. M. Kosro have been supported by grants N00014–87–K-0009 and N00014–90–J-1213. The energy and vorticity analysis software was based upon the original software graciously provided by Nadia Pinardi and Allan R. Robinson.

REFERENCES

Allen, J. S., L. J. Walstad, and P. M. Newberger, Dynamics of the coastal transition zone jet, 2, Nonlinear finite amplitude behavior, *J. Geophys. Res.*, this issue.

Bretherton, F. P., R. E. Davis, and C. B. Fandry, A technique for

objective analysis and design of oceanographic experiments applied to MODE-73, *Deep Sea Res., 23*, 559–582, 1976.

Carter, E. F., and A. R. Robinson, Analysis models for the estimation of oceanic fields, *J. Atmos. Oceanic Technol., 4*, 49–74, 1987.

Carton, J. A., How predictable are the geostrophic currents in the recirculation zone of the North Atlantic?, *J. Phys. Oceanogr., 17*, 751–762, 1987.

Denman, K. L., and H. J. Freeland, Correlation scales, objective mapping and a statistical test of geostrophy over the continental shelf, *J. Mar. Res., 43*, 517–539, 1985.

Dewey, R. K., and J. N. Moum, Enhancement of fronts by vertical mixing, *J. Geophys. Res., 95*, 9433–9445, 1990.

Flament, P., L. Armi, and L. Washburn, The evolving structure of an upwelling filament, *J. Geophys. Res., 90*, 11,765–11,778, 1985.

Haidvogel, D. B., A. R. Robinson, and E. E. Schulman, The accuracy, efficiency, and stability of three numerical models with application to open ocean problems, *J. Comput. Phys., 34*, 1–53, 1980.

Huyer, A., Hydrographic observations along the CODE central line off northern California, 1981, *J. Phys. Oceanogr., 14*, 1647–1658, 1984.

Huyer, A., P. M. Kosro, J. Fleischbein, S. R. Ramp, T. Stanton, L. Washburn, F. P. Chavez, T. J. Cowles, S. D. Pierce, and R. L. Smith, Currents and water masses of the coastal transition zone off northern California, June to August 1988, *J. Geophys. Res.*, this issue.

Kosro, M. P., A. Huyer, S. R. Ramp, R. L. Smith, F. P. Chavez, T. J. Cowles, M. R. Abbott, P. T. Strub, R. T. Barber, P. Jessen, and L. F. Small, The structure of the transition zone between coastal waters and the open ocean off northern California, winter and spring 1987, *J. Geophys. Res.*, this issue.

Miller, R. N., A. R. Robinson, and D. B. Haidvogel, A baroclinic open ocean model, *J. Comput. Phys., 50*, 38–70, 1981.

Mooers, C. N. K., and A. R. Robinson, Turbulent jets and eddies in the California current and inferred cross-shore transports, *Science, 223*, 51–53, 1984.

Paduan, J. D., and P. P. Niiler, A Lagrangian description of motion in northern California coastal transition filaments, *J. Geophys. Res., 95*, 18,095–18,109, 1990.

Pierce, S. D., J. S. Allen, and L. J. Walstad, Dynamics of the coastal transition zone jet, 1, Linear stability analysis, *J. Geophys. Res.*, this issue.

Pinardi, N., and A. R. Robinson, Quasigeostrophic energetics of open ocean regions, *Dyn. Atmos. Oceans, 10*, 185–219, 1986.

Richman, J. G., C. Wunsch, and N. G. Hogg, Space and time scales of mesoscale motion in the western North Atlantic, *Rev. Geophys. Space Phys., 15*, 385–420, 1977.

Rienecker, M. R., C. N. K. Mooers, and A. R. Robinson, Dynamical interpolation and forecast of the evolution of mesoscale features off northern California, *J. Phys. Oceanogr., 17*, 1189–1213, 1987.

Robinson, A. R. and L. J. Walstad, The Harvard open ocean model: Calibration and application to dynamical process, forecasting, and data assimilation studies, *Appl. Numer. Math., 3*, 89–131, 1987.

Robinson, A. R., M. A. Spall, and N. Pinardi, Gulf Stream simulations and the dynamics of ring and meander processes, *J. Phys. Oceanogr., 18*, 1811–1853, 1988.

Shapiro, R., Smoothing, filtering, and boundary effects, *Rev. Geophys. and Space Phys., 8*, 359–387, 1970.

Smith, J. A., C. N. K. Mooers, and A. R. Robinson, Estimation of quasi-geostrophic model amplitudes from XBT/CTD survey data, *J. Atmos. Oceanic Technol., 2*, 491–507, 1985.

Smith, R. L., G. Pittock, J. Fleischbein, and R. Still, Current measurements from moorings off northern California: September 1984 to July 1985, *Data Report 121, Reference 86-6*, College of Oceanography, Oregon State University, Corvallis, 1986.

Strub, P. T., et al., The nature of the cold filaments in the California current system, *J. Geophys. Res.*, this issue.

Walstad, L. J. and A. R. Robinson, Hindcasting and forecasting of the POLYMODE data set with the Harvard open ocean model, *J. Phys. Oceanogr., 20*, 1682–1702, 1990.

J. S. Allen, A. Huyer, P. M. Kosro, and L. J. Walstad, College of Oceanography, Ocean Admin. Bldg. 104, Oregon State University, Corvallis, OR 97331–5503.

(Received August 22, 1990;
accepted April 1, 1991.)